Chemical Science

ROYAL SOCIETY OF CHEMISTRY

PERSPECTIVE

View Article Online
View Journal | View Issue

Check for updates

Cite this: *Chem. Sci.*, 2026, **17**, 6283

All publication charges for this article have been paid for by the Royal Society of Chemistry

Received 19th January 2026
Accepted 24th February 2026

DOI: 10.1039/d6sc00523c

rsc.li/chemical-science

Architecting NIR-II metal supramolecular dyes—illuminating the path to precision medicine

Fang Zhao,†[abe] Qiao Song,†[b] Panxing Qiu,†[b] Xiaoxing Xiong,*[ac] Youjia Tang*[a] and Yao Sun *[de]

Precision medicine calls for molecular tools that enable high-resolution imaging at depth, accurate lesion localisation and controllable therapy. Small-molecule dyes are widely used in biomedical imaging and treatment, yet their limited photostability, susceptibility to quenching in physiological environments and rapid *in vivo* clearance continue to hinder clinical translation. Coordination-driven supramolecular chemistry offers a promising route to address these shortcomings. However, progress in *in vivo* delivery and biodistribution, real-time visual tracking and therapeutic evaluation has often been constrained by short-wavelength excitation and emission. In this context, second near-infrared (NIR-II) metal supramolecular dyes assembled directly from NIR-II ligands have been rapidly developed, furnishing platforms with strong NIR-II performance and tunable photophysical behaviour. This perspective summarises design and construction strategies for NIR-II metal supramolecular dyes, highlights their key photophysical characteristics, and surveys representative applications in cancer, antibacterial and cardiovascular theranostics and imaging. We further discuss outstanding challenges for clinical translation and outline future opportunities for NIR-II metal supramolecular dyes in precision medicine.

1 Introduction

Human health has been seriously threatened by various diseases including cancer, cardiovascular disorders, diabetes, chronic respiratory diseases, *etc.*[1–6] Aimed to advance personalized healthcare approaches based on individual characteristics, precision medicine launched by the American government has been repeatedly emphasized and played a critical role in public health.[7,8] Precision medicine, proposed as a top-level medical concept, aims to achieve individualized healthcare through more accurate strategies for prevention, diagnosis, treatment, and monitoring.[9,10] To advance its development, there is an urgent need for novel molecular tools capable of enabling high-resolution imaging, deep-tissue penetration, precise lesion localization, and controllable therapeutic responses within living systems.[11–16]

Small-molecule dyes have served as crucial tools in biomedicine for a long time. (*e.g.*, MB and ICG).[17–22] Nevertheless, their diagnostic and therapeutic translation remains limited by poor photostability, susceptibility to fluorescence quenching, and rapid blood clearance.[23–25] In this context, supramolecular chemistry—first introduced by the 1987 Nobel Laureates in Chemistry and further recognized by the Nobel Prizes in 2016 and 2025—has emerged as a highly promising strategy to overcome these limitations.[26–30] Supramolecular systems are generally constructed through noncovalent interactions, including hydrogen bonding, coordination interactions, π–π stacking, hydrophobic forces, and electrostatic interactions.[31–36]

Among them, metal–organic complexes (**MOCs**) represent a classical class and are constructed through coordination-driven self-assembly between Lewis basic organic ligands and Lewis acidic metal acceptors, affording well-defined two-dimensional metallacycles and three-dimensional metallacages.[37–40] This nature-inspired assembly strategy endows **MOCs** with precise sizes and geometries, positive charge, tunable cavity dimensions, and strong anti-aggregation behavior, enabling broad applications in sensing, molecular recognition, and biomedicine.[41–48] However, traditional **MOCs** still face challenges such as potential heavy-metal-induced toxicity and multidrug resistance.[49–51] To address these issues, researchers have employed small-molecule dyes as ligands to construct metal supramolecular dyes, leveraging the unique optical properties of dyes to introduce photodynamic therapy or

---

[a] *Department of Neurosurgery, Jiujiang City Key Laboratory of Cell Therapy/Human Genetic Resources Innovation Center, The First Hospital of Jiujiang City, Jiujiang 332000, China. E-mail: yjtang0808@163.com*

[b] *College of Chemistry, Central China Normal University, Wuhan, Hubei 430079, China*

[c] *Department of Neurosurgery, Renmin Hospital of Wuhan University, Wuhan 430060, China. E-mail: xiaoxingxiong@whu.edu.cn*

[d] *College of Biomedicine and Health, Huazhong Agricultural University, Wuhan 430070, China. E-mail: sunyaogbasp@mail.hzau.edu.cn*

[e] *Hubei Jiangxia Laboratory, Wuhan 430200, China*

† These authors contributed equally to this work.

photothermal therapy.[52–55] Phototherapy efficacy can be simultaneously strengthened *via* the heavy-atom effect and the well-organized discrete characteristics in turn to achieve synergistic treatment under fluorescence guidance, further bypassing their intrinsic drug-resistance barriers.[56,57] Nevertheless, most metal supramolecular dyes absorb and emit in the UV-visible region, making it difficult to activate metal supramolecular dyes in deep tissues and causing the emitted fluorescence to attenuate rapidly within biological tissues.[58–65] As a result, imaging and therapeutic efficacy at deep lesion sites are significantly compromised, hindering further clinical translation.

To improve deep-tissue applicability, NIR-II dyes have been encapsulated within **MOCs** to construct nanotheranostic platforms that exploit the intrinsic tissue-penetration advantage of the NIR-II region, thus compensating for the limitations of conventional metal supramolecular dyes.[66–68] Yet such platforms typically rely on co-encapsulation of NIR-II dyes and traditional **MOCs** without long-wavelength emission properties, inevitably suffering from particle leakage and dye escape, which disrupt synchronized imaging and therapy and prevent real-time fluorescence feedback on the **MOCs**' *in vivo* distribution. To address this critical challenge, our group and Tang's group creatively designed NIR-II-emissive ligands capable of direct coordination with metal acceptors to form NIR-II metal supramolecular dyes through coordination-driven self-assembly. This strategy integrates NIR-II FL imaging with chemo-/phototherapy in a single platform, enabling noninvasive, real-time, and *in situ* tracking of therapeutic agents, accelerating the development of precision medicine. Notably, compared with conventional NIR-II nanoparticles (NPs), such as quantum dots or rare-earth- and nanocluster-based NPs, the discrete and well-defined nature of NIR-II metal supramolecular dyes ensures intrinsic monodispersity and excellent batch-to-batch reproducibility, enabling clear structure-property correlations and more rationally tunable pharmacokinetics (potentially even renal clearance), thereby mitigating long-term toxicity concerns. By integrating the tissue-penetration advantage of NIR-II emitters and the structural advantages of supramolecular assemblies, NIR-II metal supramolecular dyes overcome the intrinsic limitations of small dyes—enhancing photostability, extending circulation time, and significantly improving early-disease imaging and therapeutic precision.

Despite significant progress in NIR-II metal supramolecular dyes, there is still a lack of comprehensive reviews and summaries on their applications in precision biomedicine. In this perspective, we summarized the latest advancements in NIR-II metal supramolecular dyes, with a focus on the design strategies (BODIPY-based, D–A–D-based, and AIE-based) and their photophysical and photochemical properties. Furthermore, we emphasize their applications in anticancer therapy, antibacterial treatment, cardiovascular therapy, and bioimaging (Scheme 1). More importantly, this review not only highlights the current challenges faced by NIR-II metal supramolecular dyes but also provides future perspectives on bridging the gap between fundamental research and clinical translation.

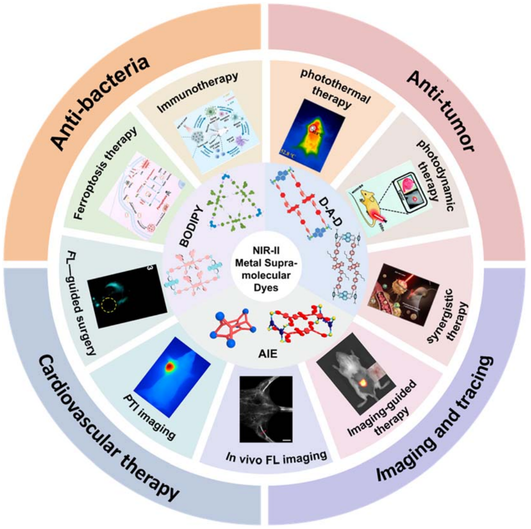

Scheme 1 Illustration of the biomedical applications of three types of NIR-II metal supramolecular dyes.

2 Construction and properties of NIR-II metal supramolecular dyes

Current design strategies for NIR-II metal supramolecular dyes primarily rely on the self-assembly of NIR-II emissive ligands with heavy metal acceptors. The inherent advantages of macrocyclic architectures effectively mitigate self-quenching, a common issue in traditional NIR-II dyes that leads to reduced fluorescence quantum yields. Without laborious synthetic steps, the photophysical behavior can be tuned in multiple dimensions by substituting ligands or metal acceptors and assembling them into metallacycles with defined geometries, thereby tailoring them for diverse biological applications. The donor ligands commonly used in NIR-II metal supramolecular dyes include aza-BODIPY, D–A–D, and AIE-based fluorophores.

2.1 NIR-II metal supramolecular dyes based on aza-BODIPY ligands

BODIPY (boron-dipyrromethene) dyes are a class of high-performance fluoroboron chromophores formed through the coordination between dipyrromethene and BF_3.[69,70] They feature excellent fluorescence quantum yields, high chemical stability, and readily modifiable structures.[71,72] However, conventional BODIPY dyes absorb and emit primarily in the visible region and exhibit small Stokes shifts.[73,74] Replacing the *meso*-carbon with nitrogen generates an aza-BODIPY core with enhanced electron deficiency, leading to further red-shifted emission.[75] Leveraging the electron-deficient framework, with the introduction of strong electron-donating groups at the α- or β-positions, D–A–D structures possessing strong electron-push–pull ability can be constructed, extending the emission into the NIR-II region (1000–1700 nm) while simultaneously improving phototherapeutic outcome.[76,77] Nevertheless, aza-BODIPY dyes still suffer from the common limitations of NIR-II fluorophores:

aggregation-caused quenching (ACQ) in aqueous media, which compromises both imaging and therapeutic efficacy.[78] Notably, constructing metal supramolecular dyes effectively suppresses ACQ. This advantage arises from the rigid macrocyclic architecture, which inherently resists quenching by preventing fluorophores from π–π stacking. Furthermore, the direct coordination of heavy atoms promotes intersystem crossing (ISC), enhancing reactive oxygen species (ROS) generation and endowing NIR-II metal–organic aza-BODIPY supramolecular dyes with excellent photodynamic therapeutic performance.

Sun and co-workers reported the first NIR-II metal supramolecular dyes based on aza-BODIPY chromophore, **Ru1085**, assembled from a bipyridine-modified aza-BODIPY ligand and a dinuclear arene–ruthenium (Ru) acceptor (Fig. 1a).[79] By introducing the strong electron-donating groups julolidine and anisole into the aza-BODIPY core, intramolecular charge transfer was significantly enhanced, shifting the emission of the ligand into the NIR-II region. **Ru1085** exhibited maximum absorption and emission at 874 nm and 1085 nm, respectively (Fig. 1b). The strong D–A–D push–pull character of the aza-BODIPY ligand, together with Ru-assisted ISC, conferred **Ru1085** with potent ROS-generating capability, which was further strengthened by the anti-quenching nature of the rigid macrocyclic scaffold (Fig. 1c). In addition, the intramolecular vibrations and charge transfer across the extended conjugated framework promoted nonradiative decay, resulting in a high photothermal conversion efficiency (PCE) of 30.9% (Fig. 1d). Further optimization of the BODIPY ligand afforded **Ru1100**, which, similar to **Ru1085**, retained NIR-II emission and excellent photothermal and photodynamic performance (Fig. 1e).[80] Together, these results established a general design strategy in which strong pull–push-electron aza-BODIPY units are embedded into rigid Ru(II) NIR-II supramolecular dyes to balance NIR-II fluorescence, ROS generation and photothermal output.

To further modulate the electronic structure and reduce Ru-induced dark reactivity, Sun and co-workers simultaneously modified both the Ru(II) acceptor and aza-BODIPY donor.[81] Based on a π-expansive strategy, acceptors **A1** and **A2** were designed to tune electron density at the Ru center, while ligands **1–3** incorporated increasingly extended nonplanar π-conjugation to strengthen spin–orbit coupling for enhanced ISC (Fig. 2a). Combinations of these motifs generated **RuA–RuD**, which exhibited red-shifted absorption (630–850 nm) and concentrated NIR-II emission (1105–1115 nm) (Fig. 2b). Notably, unlike the earlier Ru-based NIR-II supramolecular dyes, **RuA–RuD** favored type-I pathways and primarily generated superoxide anions ($^{\bullet}O_2^{-}$) under 808 nm excitation (Fig. 2c and d). The π-expanded acceptor in **RuD**, coupled with the increasing non-planar π-conjugation of the ligands, resulted in the largest steric hindrance and the smallest ΔE_{ST} (0.63 eV), which dramatically enhanced photodynamic activity while suppressing ground-state reactivity (Fig. 2e). This work provided a feasible approach to addressing biosafety of metallosupramolecular photosensitizers without compromising their photophysical performance.

Further extending this concept, Sun expanded the Ru acceptor from two units to four (**A1–A4**) to construct a series of metallacycles, **Ru1–Ru4** (Fig. 2f).[82] Systematic π-expansion around the Ru center modulated steric and electronic properties, yielding progressively enhanced ROS outputs. **Ru4**, the most π-extended system, exhibited the strongest photosensitivity and the lowest dark reactivity, reinforcing the previously proposed π-expansion as an effective design strategy for Ru-based NIR-II supramolecular dyes (Fig. 2h).

In addition to constructing Ru-based supramolecular dyes, Sun's group designed two triangular NIR-II Pt(II) supramolecular dyes using aza-BODIPY as a donor, namely **Pt1110** and **Pt1115**, respectively.[83,84] Both supramolecular dyes were

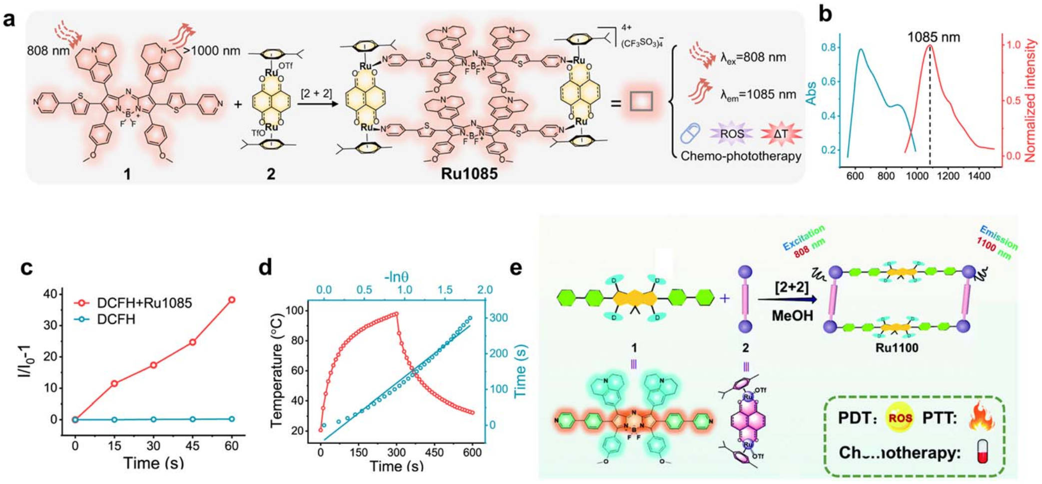

Fig. 1 (a) The design of **Ru1085**, and its photophysical properties with combined chemotherapeutic, photodynamic, and photothermal activities. (b) The UV-vis absorption and emission spectra of **Ru1085**. (c) ROS variation of **Ru1085** under 808 nm irradiation (0.8 W cm^{-2}) monitored using H2-DCFH. (d) Temperature profile of **Ru1085** under 808 nm irradiation for 300 s (red line), followed by natural cooling, and the corresponding linear plot of time *versus* −ln θ (blue line) obtained during the cooling stage. Reproduced with permission from ref. 79. Copyright 2022, Springer Nature. (e) The design of **Ru1100** and its photophysical properties. Reproduced with permission from ref. 80. Copyright 2022, Royal Society of Chemistry.

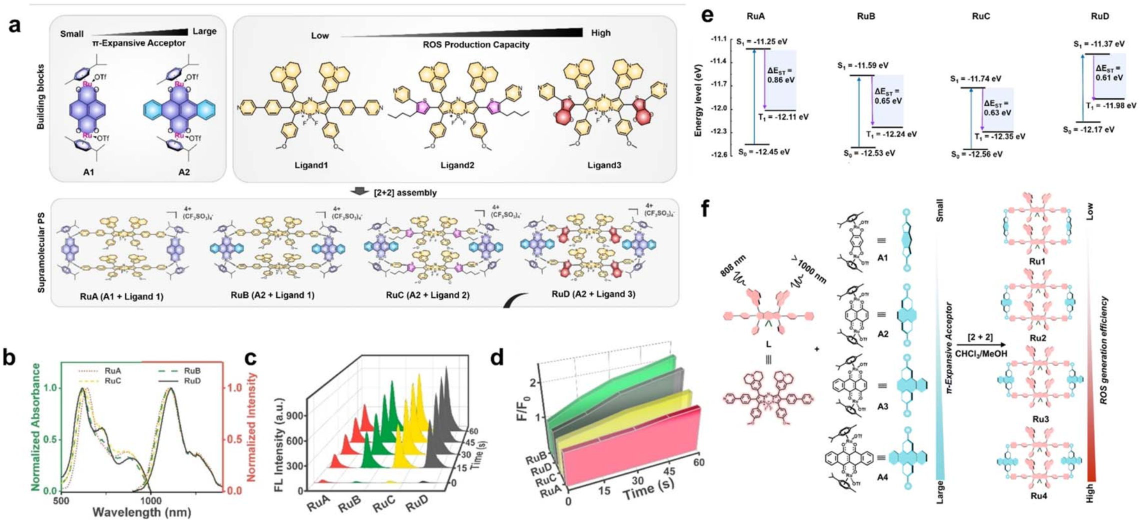

Fig. 2 (a) The design strategy of **RuA–RuD** and the illustration of chemical structures. (b) The UV-vis absorption and emission spectra of **RuA–RuD**. (c) ROS generation of **RuA–RuD** using an 808 nm laser monitored using DCFH-DA. (d) The $^{\bullet}O_2^-$ production from **RuA** to **RuD** using DHE as an indicator. (e) The calculated orbital energy level of **RuA–RuD** at B3LYP/6-31G. Reproduced with permission from ref. 81. Copyright 2023, Wiley-VCH. (f) The design strategy of **Ru1–4** and the chemical structures. Reproduced with permission from ref. 82. Copyright 2023, Royal Society of Chemistry.

assembled through [3 + 3] coordination-driven self-assembly between NIR-II aza-BODIPY dyes and the Pt(II) acceptor in dichloromethane, forming well-defined triangular two-dimensional metallacycles in a 1 : 1 molar ratio (Fig. 3a and b). Although the Pt acceptors were identical, the ligand in **Pt1110** features weaker non-planar conjugation than that in **Pt1115,** indicating its freer rotation of the covalent bond. **Pt1110** combined efficient ROS generation with a high photothermal conversion efficiency of 32.8%, making it a representative example of BODIPY-based metal supramolecular dyes that support synergistic photodynamic/photothermal outputs (Fig. 3c and d). In contrast, **Pt1115**, with six ISC channels, demonstrated a markedly enhanced ability to generate $^{\bullet}O_2^-$ (Fig. 3e and f). Additionally, due to its rigid architecture, **Pt1115** exhibits superior ROS generation efficiency and reduced ROS diffusion compared to its small-molecule counterpart (Fig. 3g). Notably, the positive charge and well-defined triangular geometry of these Pt metallacycles generally favoured retention in pathophysiological environments, thereby facilitating optimal therapeutic efficacy.

2.2 NIR-II metal supramolecular dyes based on D–A–D ligands

The D–A–D skeleton represents a special case of donor–acceptor (D–A) fluorescent molecules.[85] In this framework, electron-donating groups are typically installed at both ends, while

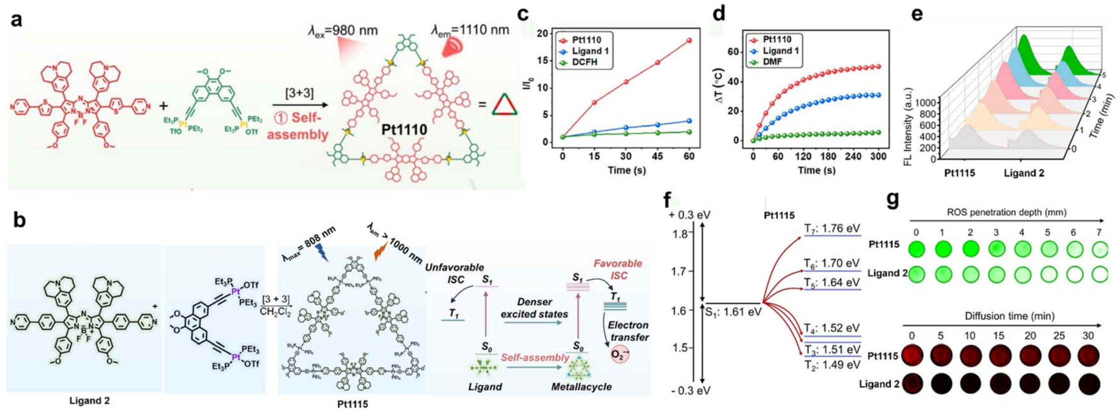

Fig. 3 (a) The preparation and design of **Pt1110**, and the illustration of optical properties. (b) The design of **Pt1115** and the displayed optical properties mechanistically before and after assembly. (c) The comparison of ROS generation for **Pt1110** and its ligand over time (indicator: DCFH). (d) The temperature profiles of **Pt1110**, ligand and DMF with irradiation time. (e) Generation of $^{\bullet}O_2^-$ of **Pt1115** and its ligand upon 808 nm laser irradiation at 1 W cm^{-2}. (f) Computed energy levels and potential ISC pathways of **Pt1115**. (g) Top: DCF fluorescence images of **Pt1115** and its ligand at different depths under 808 nm laser excitation (1 W cm^{-2}); bottom: NIR-II fluorescence images of **Pt1115** and its ligand. Reproduced with permission from ref. 83. Copyright 2023, Springer Nature. and ref. 84. Copyright 2024, Wiley-VCH.

electron-withdrawing units are positioned at the center, with the donor and acceptor interacting through conjugated linkages.[22,86] Owing to the strong intramolecular push–pull effect, D–A–D molecules possess reduced optical band gaps, in which the energy gap between the highest occupied molecular orbital (HOMO) and the lowest unoccupied molecular orbital (LUMO) is significantly lowered, shifting the emission into the NIR-II window.[87,88] D–A–D chromophores generally exhibit high chemical and photostability, large molar extinction coefficients, and large Stokes shifts.[89,90] At present, the construction of D–A–D molecules commonly employs benzobisthiadiazole as the electron-withdrawing core, while thiophene, 3,4-ethylenedioxythiophene (EDOT), furan, and related units serve as electron donors.[91] Shielding units are often incorporated to improve fluorescence quantum yields.[92] However, the multistep synthetic procedures and the often suboptimal quantum yields, even after extensive optimization, have motivated chemists to explore alternative strategies to enhance the emissive efficiency of D–A–D chromophores. In this context, the inherent structural advantages of metal supramolecular dyes offer fertile ground for further improving D–A–D molecular architectures.

Initially, Sun and Kim attempted to improve the quantum yield by encapsulating visible-light Pt-based supramolecular dyes and D–A–D dyes with DSPE-PEG5000, preparing nanoparticles.[67] However, this amphiphilic polymer-encapsulation strategy inevitably caused spatiotemporal mismatch between the fluorescence signal and the therapeutic agent. To overcome this issue, Sun developed Ru-based supramolecular dyes, **1** and **Ru1000**, featuring well-defined structures and dimensions, in which the NIR-II D–A–D dyes were directly integrated into the metal-macrocyclic platform to achieve synchronized fluorescence reporting and therapeutic function.[93,94] Both supramolecules were constructed through [2 + 2] coordination-driven self-assembly between small-molecule D–A–D ligands and dinuclear arene–Ru acceptors (Fig. 4a and b). Notably, **Ru1000** incorporated 3,4-ethylenedioxythiophene (EDOT) as the electron-donating unit, while **1** uses 3-butylthiophene. This difference resulted in a higher relative quantum yield for **Ru1000** (0.94) compared to **1** (0.46) (Fig. 4c and d), likely because the alkyl chain in **1** enhanced intramolecular vibration and favoured photothermal conversion. Under 808 nm laser irradiation, the temperature of **1** increased rapidly with concentration (>80 °C), achieving a photothermal conversion efficiency of 39%, surpassing **Ru1000** with a PCE of only 17.6% (Fig. 4e and f). In addition, both **Ru1000** and **1** exhibited appreciable photodynamic activity, supporting their application in combined chemo-phototherapy.

Building on the breakthrough of D–A–D-based metal supramolecular dyes as efficient photosensitizers, Sun's group further developed novel metal supramolecular dyes to explore their potential in sonodynamic therapy (SDT).[95,96] Following conventional strategies for enhancing photosensitizing properties, they created two high-performance Ru-based sonosensitizers, **Ru-A3-TTD** and **Ru3**. The design of **Ru-A3-TTD** primarily involved the optimization of the Ru(II) receptor (Fig. 5a). From **Ru-A1** to **Ru-A3**, the sonodynamic efficacy was gradually improved because of their progressively narrower energy gap (Fig. 5b and c). **Ru-A3** was chosen to self-assemble with a D–A–D ligand (**TTD-L**) carrying the thiazolothiazole (**TTD**) as an electron-deficient core, forming a macrocyclic structure (Fig. 5a). The assembled **Ru-A3-TTD** with NIR-II emission (880 nm) generated markedly higher levels of ROS under ultrasound (US) activation than commercial sonosensitizers such as **PpIX**, **Ce6**, and **MB** (Fig. 5d and e). The construction of **Ru3** relied on the optimization of D–A–D ligands. Extension of ligand conjugation and enhancement of the push–pull character red-shifted

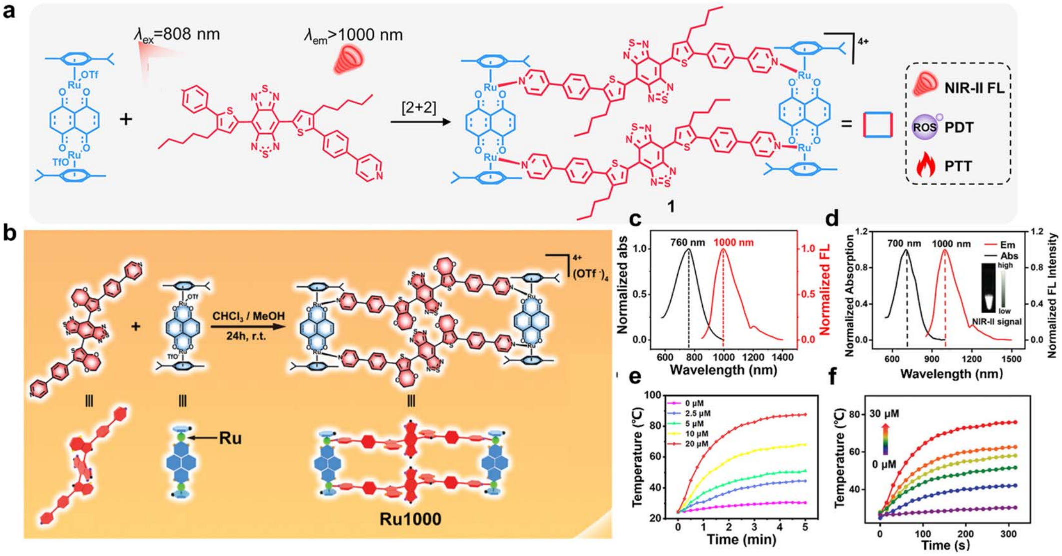

Fig. 4 (a) The self-assembly of complex **1** and its optical properties. (b) The preparation of **Ru1000**. (c) The absorption and fluorescence spectrum of complex **1**. (d) The UV-vis absorption and emissive spectra of **Ru1000** and its NIR-II FL image under 808 nm irradiation. Temperature change curves of complex **1** (e) and **Ru1000** (f) at different concentrations under 808 nm laser irradiation (0.8 W cm^{-2} for complex **1** and 1 W cm^{-2} for **Ru1000**). Reproduced with permission from ref. 93. Copyright 2022, Proceedings of the National Academy of Sciences of the United States of America and ref. 94. Copyright 2022, Wiley-VCH.

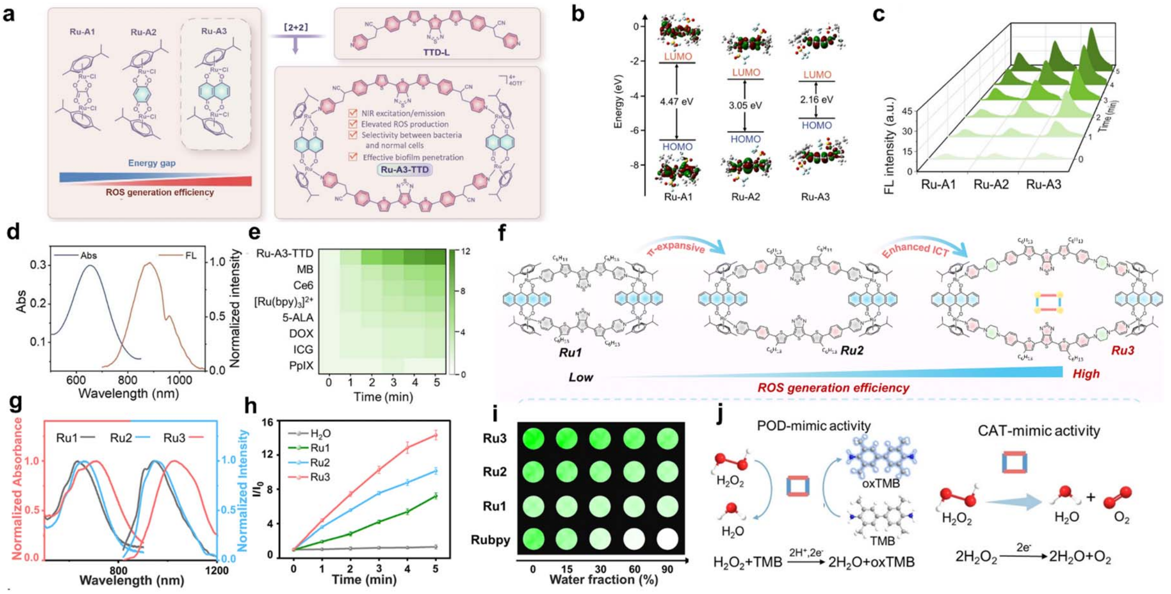

Fig. 5 (a) Diagram depicting the design strategy of **Ru-A3-TTD**. (b) The electron density distribution in the LUMO–HOMO of **Ru-A1**, **Ru-A2** and **Ru-A3**. (c) The comparison of ROS generation for **Ru-A1**, **Ru-A2** and **Ru-A3** in DMF under US irradiation with DCFH as an indicator. (d) Normalized absorption and emission spectra (λ_{ex} = 690 nm) of **Ru-A3-TTD** in DMSO. (e) Heat map of relative fluorescence intensity changes of **DCFH** recorded at 525 nm in the presence of **Ru-A3-TTD** and other commercial sonosensitizers at different US irradiation times. Reproduced with permission from ref. 95. Copyright 2024, Wiley-VCH. (f) Schematic illustration of the design strategy to improve sonodynamic efficacy. (g) Normalized absorption spectra and the emission spectra (λ_{ex} = 808 nm) of **Ru1–Ru3** in DMSO. (h) DCF fluorescence intensity changes in the presence of **Ru1–Ru3** under US irradiation. (i) Fluorescence images of DCFH indicating ROS production from **Ru1–Ru3** in mixed DMF/H_2O solutions with varying ratios under US irradiation. (j) POD-mimic (left) and CAT-mimic (right) activities of **Ru-A3-TTD** and **Ru3**. Reproduced with permission from ref. 96. Copyright 2025, Royal Society of Chemistry.

the maximum emission of **Ru3** to 1032 nm and exhibited the highest level of ROS generation within the series (Fig. 5h and i). Under US irradiation, **Ru3** displayed a singlet oxygen ($^1O_2$) quantum yield (Φ_Δ) of 0.89. In contrast to Rubpy, the ROS output of **Ru3** remains essentially unchanged upon increasing water content, which is attributed to its rigid framework and the steric hindrance around the Ru acceptor (Fig. 5j). More importantly, the half-hourglass Ru(II) acceptor endows **Ru-A3-TTD** and **Ru3** with pronounced enzyme-mimetic and sonocatalytic activities, enabling it to enhance ROS production through CAT- and POD-like catalysis while simultaneously depleting GSH and oxidizing NADPH (Fig. 5k and l), which collectively strengthened its potential as an efficient sonosensitizer for biotherapy. These findings highlighted that fine-tuning the donor–acceptor balance, conjugation length, and macrocyclic rigidity in D–A–D-type metal supramolecular dyes significantly influenced their electronic properties and ROS generation efficiency. Such structure-property understanding provides valuable design principles for developing multimodal metal–organic sensitizers with controllable redox and energy-transfer properties.

2.3 NIR-II metal supramolecular dyes based on AIE ligands

Due to the relatively planar structures of traditional NIR-II fluorophores, supramolecular metal dyes tend to aggregate in aqueous solutions, leading to aggregation-caused quenching (ACQ) and resulting in weak or even negligible fluorescence. This phenomenon significantly hampers the application of supramolecular metal dyes in biological systems. Aggregation-induced emission (AIE) scaffolds, first proposed by Ben Zhong Tang in 2001, are a class of unique molecular fluorophores that exhibit drastically enhanced fluorescence in the aggregated state.[97–99] Clearly, utilizing AIE luminogens as building blocks for the construction of AIE-based metal supramolecular dyes holds significant promise for improving diagnostic and therapeutic efficacy.

To verify the feasibility of constructing an AIE-active NIR-II metal supramolecular dye, Tang *et al.* reported an AIE-emissive metallacage, **C-DTTP**, assembled from a four-armed AIE-active NIR-II ligand (DTTP) and a 90° Pt(II) acceptor ($Pt(PEt_3)_2(OTf)_2$), in a 1 : 2 molar ratio (Fig. 6a).[100] Displaying a low-symmetry prismatic conformation, **C-DTTP** exhibited two absorption peaks at 368 nm and 675 nm, corresponding to π–π* transitions and charge-transfer processes, respectively (Fig. 6b). The fluorescence region of **C-DTTP** was centered at 800–1250 nm (maximum at 1005 nm) and displayed a pronounced AIE enhancement as the toluene fraction increased in DMSO/toluene mixtures (Fig. 6c). Compared with its ligand, **C-DTTP** not only exhibited a considerable photothermal effect (69 °C) under laser irradiation but also showed enhanced ROS generation, attributed to its hollow structure facilitating oxygen diffusion, rigid cage framework resisting ROS quenching, and the heavy-atom induced ISC from the Pt(II) center (Fig. 6d and e). To improve the dispersibility and stability of the hydrophobic cage in aqueous media, the researchers encapsulated it using an amphiphilic polymer (mPEG-PLGA), forming **CNPs**. According to the energy gap theory, red-

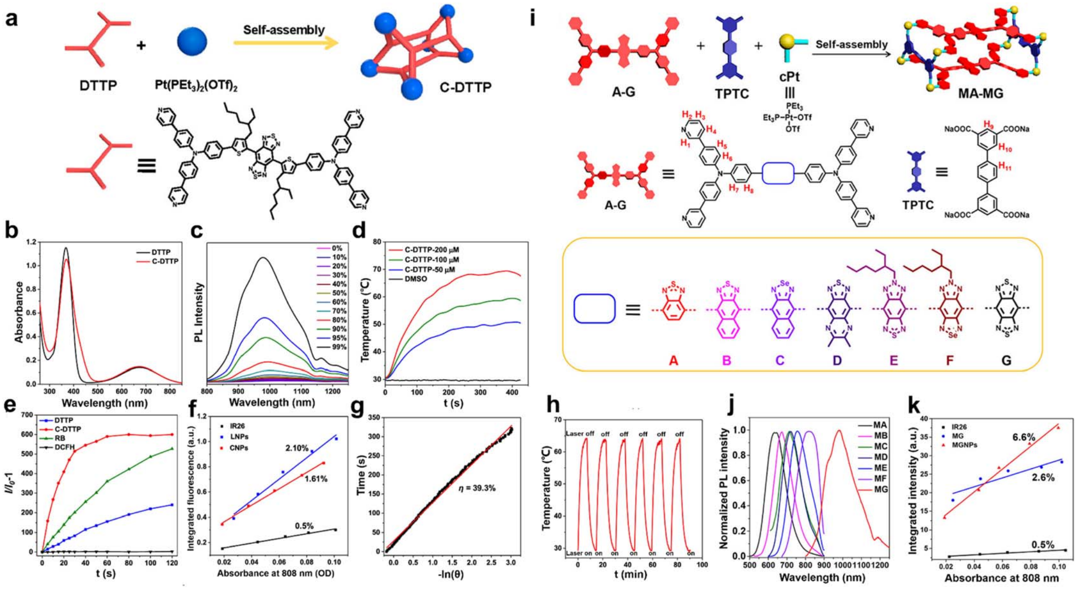

Fig. 6 (a) Self-Assembly of **C-DTTP**, with the demonstration of the ligand structure and shape of **C-DTTP**. (b) Absorption spectra of **DTTP** and **C-DTTP**. (c) Photoluminescence spectra of **C-DTTP** recorded in DMSO/toluene mixed solvents with varying toluene content. (d) The temperature profiles of **C-DTTP** at different concentrations under 808 nm laser irradiation (0.8 W cm^{-2}). (e) ROS generation of **C-DTTP** compared with that of **DTTP** and **RB** using DCFH as an indicator under 808 nm laser irradiation (0.8 W cm^{-2}). (f) NIR-II fluorescence quantum yields of **CNPs** (encapsulated **C-DTTP**). (g) Photothermal conversion efficiency of **CNPs**. (h) Photothermal stability of **CNPs** undergoing six heating-cooling cycles. Reproduced with permission from ref. 100. Copyright 2022, American Chemical Society. (i) The design and preparation of box-like NIR-II metal supramolecular dyes (**MA–MG**) with a tunable NIR-II emission wavelength. (j) Normalized emission spectra of **MA–MG**. (k) NIR-II fluorescence quantum yields of **MG** and **MGNPs** relative to **IR26**. Reproduced with permission from ref. 101. Copyright 2023, American Chemical Society.

shifting the emission wavelength into the NIR region typically decreases quantum yield. However, **CNPs** exhibited a remarkably high absolute quantum yield of 1.3%, significantly higher than that of carbon nanotubes (0.4%) and IR26 (0.5%) (Fig. 6f). Furthermore, the **CNPs** demonstrated an impressive photothermal conversion efficiency of 39.3% with excellent photothermal stability (Fig. 6g and h). Collectively, these results highlighted the great potential of **CNPs** as NIR-II imaging and therapeutic agents for *in vivo* applications.

By removing the alkyl chain of thiophene in **C-DTTP**, Tang's group developed an AIE-based NIR-II prismatic metallacage (**M-DBTP**) for long-term monitoring of Pt distribution and metabolism *in vivo*.[101] The integrated metallacage architecture allowed simultaneous visualization of Pt while retaining bright, stable, and high-contrast imaging performance over extended periods. The rigidity of the metallacage effectively restricted the internal rotation of ligand molecules, significantly enhancing the AIE performance in both aggregated and nanoparticle states. Compared with the free ligand, **M-DBTP** displayed an enhanced fluorescence quantum yield, and upon encapsulation into nanoparticles (**M-DBTP NPs**), the absolute quantum yield further increased to 1.1%, providing a solid foundation for long-term *in vivo* fluorescence analysis.

Following the demonstration of **C-DTTP** as a prototypical NIR-II AIE metal supramolecular dye, Tang's group advanced this concept by incorporating AIE units with various D–A–D skeletons to achieve controllable emission tuning of AIE-active cages in the long-wavelength region. They successfully constructed a series of NIR-II supramolecular cages (**MA–MG**) with AIE activity and tunable fluorescence (Fig. 6i).[102] **MA–MG** were constructed *via* coordination-driven self-assembly of tetrapyridyl ligands **A–G**, a tetracarboxylic acid ligand (TPTC), and a 90° platinum acceptor Pt $(PEt_3)_2(OTf)_2$ (cPt), forming box-like architectures. Among them, **MG** exhibited the maximum emission at 980 nm (Fig. 6j) and an evident AIE effect. The encapsulated **MG** nanoparticles (**MGNPs**) showed excellent stability and an absolute quantum yield of 1.3%, surpassing that of commercial NIR-II imaging agents such as **CH1055-PEG** (0.3%) (Fig. 6k). This outstanding performance underscored the promise of AIE-active NIR-II metal supramolecular dyes as next-generation NIR-II emitters for deep-tissue optical imaging.

On the whole, these three types of NIR-II metal supramolecular dyes each offer unique advantages, accompanied by corresponding challenges. They all demonstrated efficient ROS generation enabled by metal-assisted ISC and enhanced fluorescence mediated by anti-quenching of the rigid structure. Aza-BODIPY-based systems, benefiting from a well-established chromophore platform, possess high molar absorptivity and robust stability, although achieving deep NIR-II emission typically requires strong push–pull engineering. D–A–D-based ones, characterized by narrow band gaps and strong intramolecular charge transfer, facilitate red-shifted emission and multimodal therapeutic functions, including PDT and PTT, yet their synthetic complexity and sensitivity to structural modification often render emission efficiency vulnerable to nonradiative decay. AIE-based systems convert aggregation into an advantage, dramatically enhancing fluorescence performance in aqueous environments and mitigating ACQ. However, achieving simultaneously high quantum yield and long-wavelength NIR-II emission remains intrinsically challenging according to the energy gap law. Additionally, the large architectures of metal cages may influence pharmacokinetics and metabolic behavior. Together, these three strategies provide complementary tools for tuning imaging depth, ROS output, and therapeutic functionality based on specific application needs.

3 Application of NIR-II metal supramolecular dyes in precision medicine

3.1 NIR-II metal supramolecular dyes for cancer therapy

Photodynamic therapy (PDT), as a means for tumor treatment, possesses non-invasiveness and spatiotemporal controllability.[103–105] However, its clinical translation remains limited by the intrinsic drawbacks of conventional photosensitizers, including suboptimal excitation wavelengths, inherent dark toxicity, and poor efficacy in hypoxic tumor microenvironments.[106–108] To address these challenges, metal supramolecular dyes have emerged as an ideal platform for constructing novel photosensitizers (PSs) due to their advantages such as tunable structures, ease of integrating functional units, and the ability of the metal center to promote ISC to enhance ROS generation.

Ru(II) complexes have found widespread application in the field of PDT. However, excitation/emission spectra of Ru(II) complexes are currently mainly concentrated in the short-wavelength-emissive region. This not only diminishes the efficiency of phototherapy but also hinders real-time monitoring of therapeutic effects in deep tissues. For this reason, Sun developed an NIR-II Ru(II) supramolecular dye (**Ru1085**), which demonstrated potent *in vivo* anti-tumor activity (Fig. 7a).[79] Benefiting from the great lipophilicity stemmed from the macrocycle structure, **Ru1085** can be efficiently taken up by A549 cells and mainly enriched in lysosomes, with a Pearson correlation coefficient (PCC) as high as 0.71 (Fig. 7b). Besides, it was partially distributed in mitochondria owing to the carried positive charge. Using 808 nm irradiation, **Ru1085** produced ROS abundantly in the cells and activated the downstream expression of caspase 3/7 mediated by mitochondria (Fig. 7c–e). Flow cytometry analysis indicated that **Ru1085** mainly induced early apoptosis, while after laser irradiation, apoptosis was mainly late and necrotic (Fig. 7f). The NIR-II emission endows it with high imaging quality and ideal spatial resolution *in vivo*, with a signal-to-background ratio (SBR) as high as 13.6 (Fig. 7g and h). What is more, the nanoparticles **Ru1085 NPs** coated with DSPE-PEG5000 can effectively inhibit tumor growth *via* synergetic chemo-phototherapy (Fig. 7i). This study elucidated the anti-tumor mechanism of **Ru1085**, opening the way for metal supramolecular dyes as metal agents with the function of fluorescence-guided synergistic therapy for cancer therapy.

Building on the favorable therapeutic performance of **Ru1085**, Sun and co-workers further developed another NIR-II

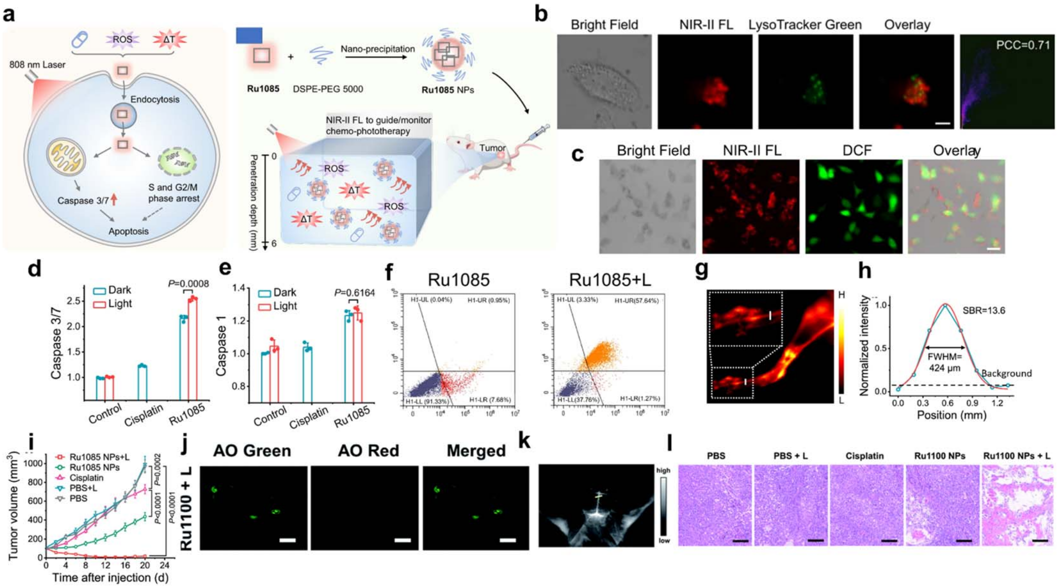

Fig. 7 (a) The antitumor mechanism involves endocytic uptake of **Ru1085** by A549 cells, leading to mitochondria-mediated apoptosis and cell-cycle cessation in the S and G2/M phases. (b) Colocalization assessment of **Ru1085** with lysosomes using LysoTracker Green. Scale bar, 5 μm. (c) DCFH-DA stained cells treated with **Ru1085** under laser illumination (808 nm). Scale bar, 20 μm. Expression levels of caspase 3/7 (d) and caspase 1 (e) after various treatments. (f) Flow cytometer results of Annexin V-FITC/PI double-stained cells treated with **Ru1085** and **Ru1085** + L. (g and h) NIR-II fluorescence images of hindlimb vessels treated with **Ru1085 NPs**. (i) Tumor volume profiles after treatment with different groups. Reproduced with permission from ref. 79. Copyright 2022, Springer Nature. (j) Confocal images of acridine orange (AO) stained A549 cells incubated with **Ru1100** under laser irradiation (808 nm). Scale bar: 20 mm. (k) NIR-II FL image of brain vessels within **Ru1100 NPs**. (l) H&E staining of A549 tumour slices with different groups. Reproduced with permission from ref. 80. Copyright 2022, Royal Society of Chemistry.

Ru-based supramolecular dye (**Ru1100**) as a substitute for conventional Pt(II) chemotherapeutics, which are often limited by dose-dependent side effects and drug resistance.[80] Owing to lipophilicity ascribed by the rigid macrocycle, **Ru1100** showcased similar colocalization sites to **Ru1085**, primarily in the lysosome. The way of **Ru1100** killing cancer cells was through destroying the integrity of lysosomal function to induce lysosomal damage (Fig. 7j). **Ru1100** served to arrest the cell cycle mainly in the G2/M phase. *In vivo* experiments have shown that after injecting **Ru1100** NPs into mice for 1 h, non-invasive visualization of the cerebrovascular network can be achieved through the complete scalp and skull, resulting in clear images with a high SBR (4.8) (Fig. 7k). Notably, **Ru1100** showed pronounced chemo-phototherapy performance in A549 xenograft models without damage to the normal physiological organs of mice (Fig. 7l).

Sun's group summarized patterns and found that the NIR-II metal supramolecular dyes adopted with dinucleararene Ru as an acceptor typically showed low phototoxicity indices (PIs), which severely restricted their clinical translation. They constructed a series of NIR-II Ru(II) supramolecular dyes (**RuA–RuD**) in search of metal agents with an optimal PI. Owing to the enlarged conjugated plane of the Ru(II) acceptor, **RuD** showed reduced dark toxicity by steric bulk blocking the Ru center from interactions with biomacromolecules (Fig. 8a).[81] Under 808 nm laser irradiation, **RuD** efficiently induced ROS production in A549 cells under both normoxic and hypoxic conditions, verifying its potential in the hypoxic tumor microenvironment (Fig. 8b). In the cellular uptake experiment, **RuD** demonstrated better selectivity for cancer cells compared to normal cells and was primarily localized in the lysosomes (Fig. 8c). Moreover, **RuD** exhibited excellent tumor penetration ability (Fig. 8d). Exploring the concrete anti-cancer process, they discovered that **RuD** under light irradiation induced mitochondrial membrane depolarization and lysosomal dysfunction, ultimately leading to cancer cell death. It mainly blocks the cancer cells in the G2/M phase and induced apoptosis by activating caspase 3 to inhibit the growth of tumor cells. *In vivo* experiments verified that **RuD** significantly inhibited the tumor growth without causing adverse effects on normal physiological functions in mice.

Inspired by the excellent performance presented by **RuD**, Sun pioneered a series of Ru(II) supramolecular dyes (**Ru1–Ru4**) *via* a receptor π expansion strategy to further investigate the how metal supramolecular dyes influence dark toxicity (Fig. 8e).[82] With the enhancement of π-conjugation in the Ru acceptors, the metallacycles demonstrated an increased capability for ROS generation and a superior shielding effect. Among them, **Ru4** demonstrated excellent cellular uptake, 2–3 times that of **Ru1–Ru3** (Fig. 8f), with the PI value reaching as high as 146. Consistent with **RuD**, **Ru4** effectively inhibited tumor growth under 808 nm laser irradiation without noticeable adverse effects on body weight or major organs, demonstrating its excellent therapeutic efficacy and biocompatibility *in vivo*.

The aforementioned NIR-II metal supramolecular dyes shone in the precise biological application because of their remarkable therapeutic efficacy and excellent biosafety *in vivo*.

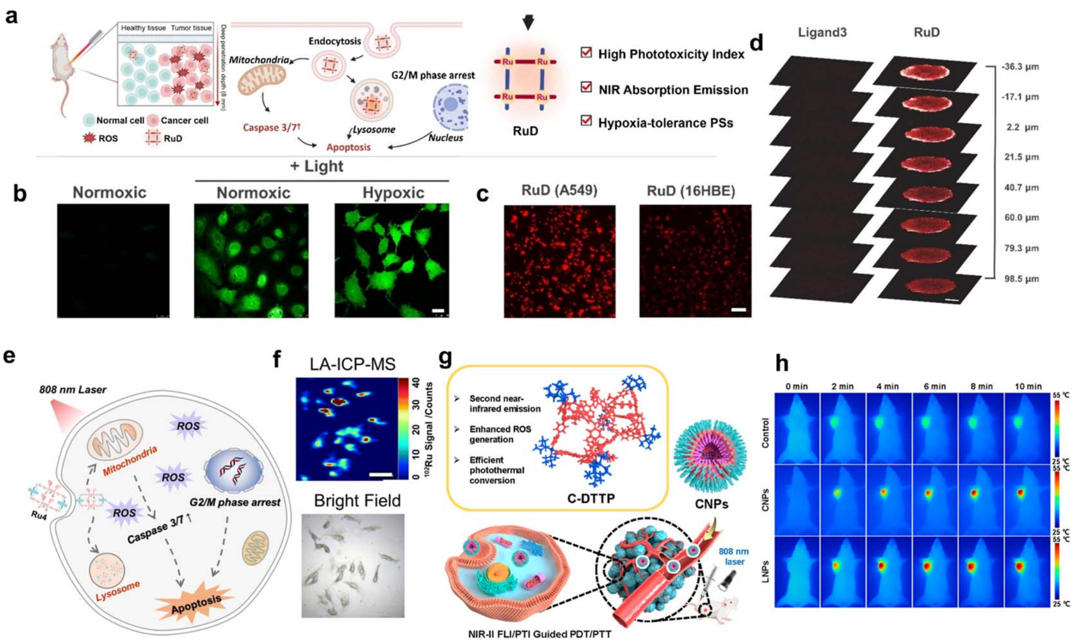

Fig. 8 (a) The antitumor mechanisms of **RuD**. (b) Confocal images of DCFH-DA stained A549 cells treated with **RuD** and irradiation (808 nm). Scale bar, 25 μm. (c) NIR-II fluorescence images of A549 cells and 16HBE cells treated with **RuD** for 12 h, demonstrating its selective uptake. Scale bar, 100 μm. (d) Confocal microscopy images of A549 multicellular tumor spheroids after incubation with **RuD** and Ligand3. Reproduced with permission from ref. 81. Copyright 2023, Wiley-VCH. (e) The antitumor mechanisms of **Ru4**. (f) LA-ICP-MS images showing the content of ^{102}Ru in A549 cells after incubation with **Ru4**. Scale bar: 50 mm. Reproduced with permission from ref. 82. Copyright 2023, Royal Society of Chemistry. (g) NIR-II anti-tumor PDT/PTT guided by FL/PTI induced by **CNPs**. (h) Thermal images of tumor-bearing mice under continuous 808 nm laser irradiation for different times in different groups. Reproduced with permission from ref. 100. Copyright 2022, American Chemical Society.

However, the ligands in these systems generally suffer from ACQ, leading to a moderate fluorescence quantum yield. To address this, a three-dimensional metal supramolecular dye, **C-DTTP**, with intrinsic AIE characteristics, was designed for NIR-II fluorescence (FL) and photothermal imaging (PTI)-guided phototherapy (Fig. 8g).[100] The corresponding encapsulated nanoparticles **CNPs** displayed efficient ROS generation, high photothermal conversion and photothermal stability. MTT experiments verified the potent killing cell ability compared to the ligand-encapsulated nanoparticles **LNPs**. *In vivo* imaging-guided phototherapy was conducted on tumor-bearing mice. The temperature of mice treated with **CNPs** increased by 21.3 °C, as monitored *via* PTI imaging (Fig. 8h). Moreover, the combined photodynamic and photothermal synergistic therapy (PDT&PTT) mediated by **CNPs** significantly inhibited tumor growth while retaining low systemic toxicity in treated mice.

Single-modality cancer therapies, such as chemotherapy or photodynamic therapy, often exhibit limited clinical efficacy and rarely achieve optimal therapeutic outcomes, frequently leading to tumor recurrence or metastasis. Immunogenic cell death (ICD) has emerged as a promising antitumor immunotherapy strategy that induces programmed death of malignant cells while triggering a durable, immune-mediated antitumor response, thereby effectively preventing tumor relapse and dissemination. Conventional platinum-based chemotherapeutic agents, such as oxaliplatin, induce effective ICD which typically requires high drug concentrations (~300 μM), which inevitably cause unpredictable toxicity to healthy organs. These prompted us to exploit new metal agents for efficient immunogenic cell death.

To further explore the potential of NIR-II metal supramolecular dyes in immunotherapy, Sun and co-workers designed a NIR-light-activated triangular Pt(II) supramolecular dye (**Pt1115**) as an ICD inducer for chemo-photoimmunotherapy of deep-seated tumors (Fig. 9a).[84] **Pt1115** can easily penetrate into tumor spheroids, exhibiting strong NIR-II fluorescence at a depth of 150 μm and generating substantial amounts of ROS internally (Fig. 9b). The photo-induced ROS generation mainly involved $^{\bullet}O_2^{-}$. Upon laser activation, **Pt1115** significantly upregulated calreticulin (CRT) exposure, high-mobility group box 1 (HMGB1) release, and adenosine triphosphate (ATP) secretion, confirming its ability to induce immunogenic cell death (ICD) at the cellular level (Fig. 9c). Flow cytometry analysis further revealed that laser-irradiated **Pt1115** markedly promoted CD8$^+$ T-cell infiltration and activation within tumor tissues, thereby enhancing immune-mediated antitumor responses. In parallel, it increased the proportion of CD4$^+$ T cells while suppressing Foxp3+ regulatory T cells, alleviating immunosuppression and improving therapeutic outcomes. Animal studies further demonstrated that laser-irradiated **Pt1115** effectively triggered local immune activation, leading to tumor elimination and a robust systemic antitumor immune response (Fig. 9d).

After establishing the potential of NIR-II Pt(II) supramolecular dyes as ICD inducers, Sun and co-workers further

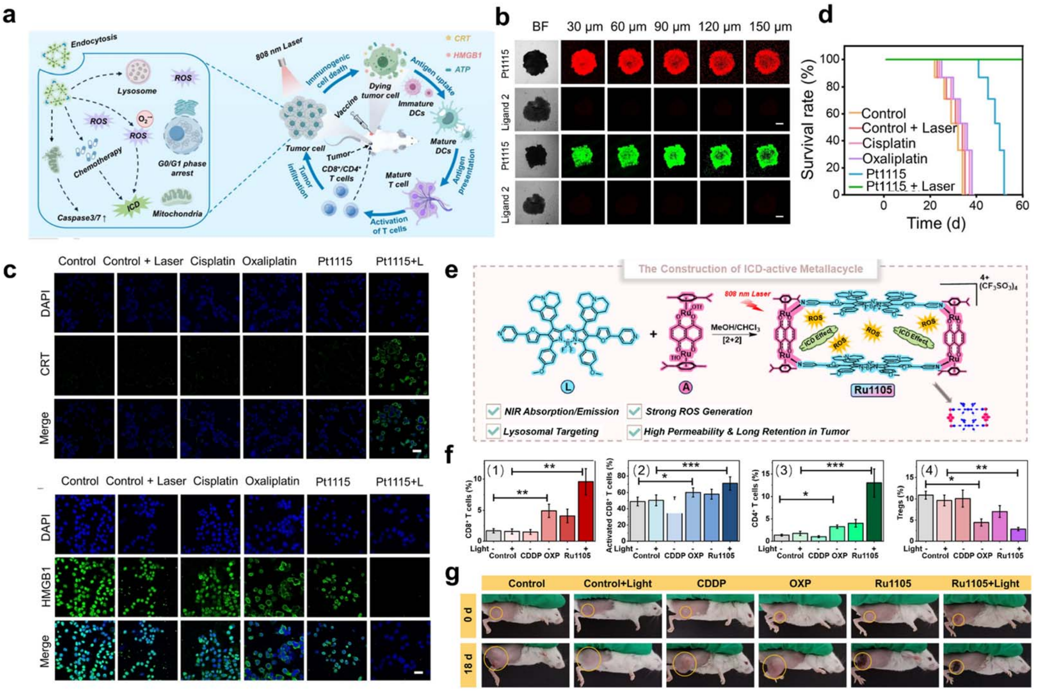

Fig. 9 (a) Illustration of the mechanism of **Pt1115** as an ICD inducer to trigger immunogenic cancer cell death. (b) Confocal microscopy images of 4T1 multicellular tumor spheroids after incubation with **Pt1115** and its ligand **2**. Scale bar: 250 μm. (c) Confocal microscopy images of surface CRT and HMGB1 release from 4T1 cells after different treatments. Scale bar: 25 μm. (d) Survival rate of 4T1 tumor-bearing mice after various treatments. Reproduced with permission from ref. 84. Copyright 2024, Wiley-VCH. (e) Schematic illustration of the preparation of **Ru1105**. (f) Quantitative assessment of the proportions of (1) CD8$^+$ T cells, (2) activated CD8$^+$ T cells, (3) CD4$^+$ T cells, and (4) Foxp3$^+$ T cells within the total tumor cell population in mice. (g) The change in tumors of the mice in different groups. Yellow circles show the tumor sites. Reproduced with permission from ref. 109. Copyright 2024, American Chemical Society.

questioned whether other heavy-metal systems could achieve comparable or even superior immunogenic cell death efficacy. They subsequently designed a Ru-based NIR-II supramolecular dye, **Ru1105**, and surprisingly found that it also elicited a strong immune response for deep-seated tumors (Fig. 9e).[109] **Ru1105** was constructed *via* coordination-driven self-assembly between a BODIPY ligand and a dinuclear arene–ruthenium acceptor, forming a ring-supported, quasi-quadrilateral metallacycle. It displays excitation and emission bands located in the NIR and NIR-II regions, respectively, enabling effective photoactivation within deep tissues. Similar to the Pt complex, **Ru1105** exhibits excellent ROS generation capability, primarily producing $^{\bullet}O_2^{-}$. Remarkably, it retains potent cytotoxicity even against hypoxic cancer cell lines under 808 nm laser irradiation, with therapeutic efficacy surpassing that of cisplatin and oxaliplatin. Due to its positive charge and moderate lipophilicity, **Ru1105** is selectively internalized by cancer cells through an endocytosis-mediated pathway while causing negligible effects on normal cells. Compared with its free ligand, **Ru1105** effectively triggered HMGB1 and ATP release in HeLa and CT26 cells and induced significant CRT exposure at concentrations as low as 10 μM—an effect unattainable by oxaliplatin even at 300 μM. Flow cytometric analysis of immune cells from vaccinated mice revealed that the combination of **Ru1105** and 808 nm laser irradiation markedly increased the populations of cytotoxic T cells and CD4^{+} T cells, while downregulating Foxp3^{+} regulatory T cells, indicating strong induction of ICD and substantial tumor inhibition with minimal tissue damage (Fig. 9f). Subcutaneous tumor models further confirmed the pronounced therapeutic efficacy of **Ru1105**, with treated mice exhibiting prolonged survival up to 60 days (Fig. 9g).

3.2 NIR-II metal supramolecular dyes for anti-bacterial therapy

NIR-II metal supramolecular dyes are widely used in tumor diagnosis and therapy, but their antibacterial applications remain in the early stages of research.[110,111] With the growing severity of antibiotic resistance, the development of novel antibacterial strategies has become an urgent priority.[112,113] Although photodynamic therapy offers advantages such as spatiotemporal controllability and a low propensity to induce drug resistance, its clinical application still faces several challenges, including limited tissue penetration depth of photosensitizers, suboptimal phototherapeutic efficiency, and potential laser safety risks.[114–116] To break through these bottlenecks, Sun's team designed and synthesized a novel Pt(II) metal supramolecular dye, **Pt1110**, and successfully applied it in antibacterial therapy research.[83] It achieved inhibition rates exceeding 98% against Gram-positive bacteria (*e.g.*, *Staphylococcus aureus*) under safe laser irradiation, revealing its remarkable anti-bacterial activity. In the mouse model of *Staphylococcus aureus* keratitis, the intravenously injected **Pt1110** NPs could target and accumulate at the infected corneal site *via* a macrophage-mediated "carrier" effect (Fig. 10a). After 12 days of treatment, the **Pt1110** NP treatment group showed significant alleviation of corneal inflammation and a substantial reduction in bacterial load (by 2.1 orders of magnitude) (Fig. 10b). The experimental results fully confirmed that the **Pt1110** material can effectively overcome the limitations of traditional photodynamic therapy, demonstrating excellent anti-infective performance in various complex biological environments, thus providing an important reference for the development of new antibacterial agents.

Subsequently, they developed a D–A–D-based Ru(II) metal supramolecular dye (**1**), with a ~1000 nm emission wavelength for antibacterial therapy.[93] It allowed deeper tissue penetration (7 mm) when compared with **Pt1110.** This complex exhibits excellent antibacterial activity against both Gram-positive (*Staphylococcus aureus*) and Gram-negative (*Escherichia coli*) bacteria, with stronger activity against Gram-positive strains (Fig. 10c). This enhanced effect is attributed to the relatively simpler cell wall structure of Gram-positive bacteria, which facilitates better penetration of the complex. Further direct evidence from scanning electron microscopy shows that the complex, upon laser irradiation, induced significant wrinkling and deformation of bacterial cell walls, ultimately leading to bacterial death (Fig. 10d). In the *S. aureus*-infected wound model, the complex **1** specifically accumulated at the infected site, promoting efficient wound healing within 6 days, significantly outperforming the control group (Fig. 10e and f).

Photodynamic therapy for biofilm infections is currently limited by the depth of penetration, while SDT can overcome this problem. Based on this, Sun systematically evaluated the great potential of **Ru-A3-TTD** in combating biofilm infections caused by multidrug-resistant bacteria.[95] The combination of positive charges and appropriate size made **RuA3-TTD** highly permeable and accumulate in biofilms. **Ru-A3-TTD** could efficiently eradicate mature biofilms under US (Fig. 10g and h). This effect was attributed to its effective penetration into the interior of biofilms and the unique triple synergistic mechanism: Establishing a wound model of MDR *E. coli* (multidrug-resistant *Escherichia coli*) biofilm infection, it was found that the infected wounds of mice in the **Ru-A3-TTD** + US group healed almost completely after an 8-day treatment and the bacterial load was reduced by approximately 5.8 orders of magnitude (Fig. 10i and j). The therapeutic effect far exceeded that of other control groups, and it had extremely high biological safety. **Ru-A3-TTD** not only successfully transformed the deep penetration advantage of sonodynamic therapy into actual therapeutic effects, but also achieved efficient and safe eradication of drug-resistant biofilm infections in the complex *in vivo* environment through its unique BME adaptive ability, demonstrating great clinical transformation prospects.

3.3 NIR-II metal supramolecular dyes for cardiovascular therapy

Recent research on NIR-II metal supramolecular dyes has primarily focused on cancer therapy and antibacterial applications. These materials can efficiently generate ROS through photodynamic or sonodynamic processes at deep tissues, inducing apoptosis of cancer cells or bacterial clearance for precision therapy. Given the critical roles of ROS in both

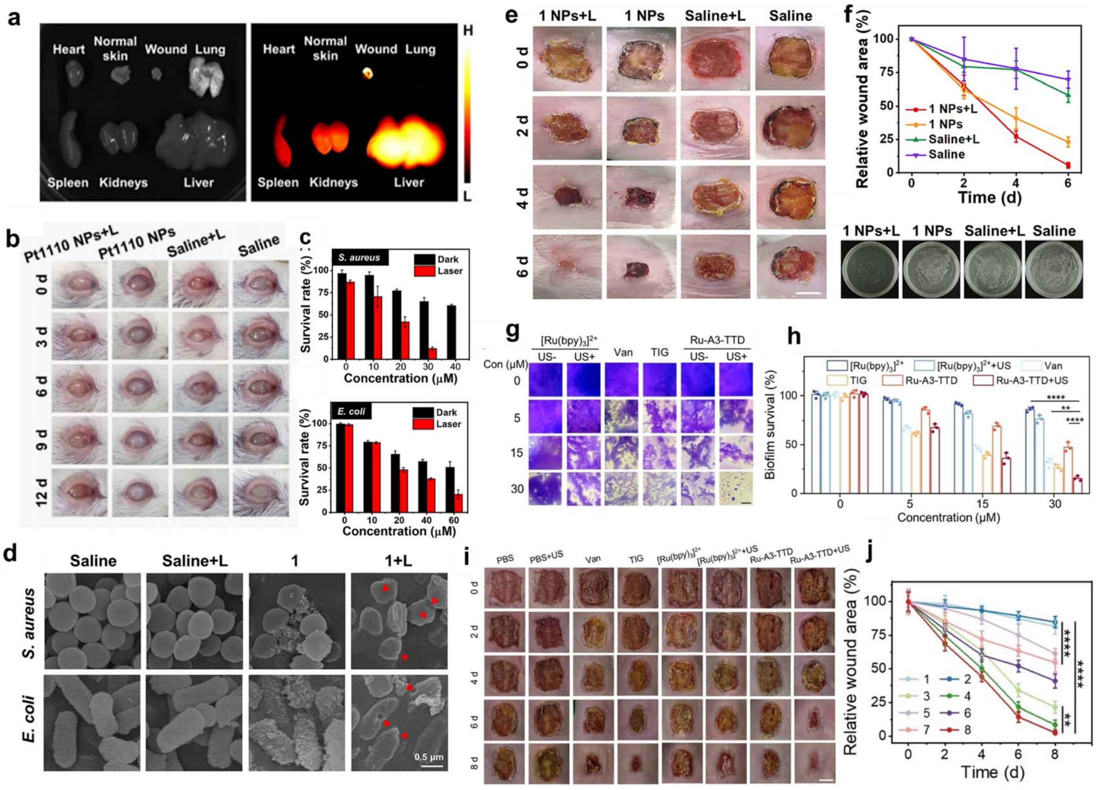

Fig. 10 (a) *Ex vivo* NIR-II fluorescence images of the wound, normal skin, and major organs from the *A. aureus*-infected mouse model 24 h after **Pt1110** NP injection. (b) Photographs of infected eyes with various treatments. Reproduced with permission from ref. 83. Copyright 2023, Springer Nature. (c) Survival rates of (top) *S. aureus* and (bottom) *E. coli* treated with different concentrations of **1** in the dark or under 808 nm irradiation (0.8 W cm^{-2}). (d) SEM images of *S. aureus* and *E. coli* after different treatments. Scale bar: 0.5 μm. (e) The photographs recording the *S. aureus*-infected wound of mice after various treatments. (f) Quantitative analysis of wound area change (top) and *S. aureus* bacterial colonies from (e) at 6 d. Scale bar, 5 mm. Reproduced with permission from ref. 93. Copyright 2022, Proceedings of the National Academy of Sciences of the United States of America. (g) Micrographs of crystal violet-stained biofilms incubated with **Ru-A3-TTD**, with or without US irradiation. Scale bar: 200 μm. (h) Relative survival of biofilms under different treatments. (i) Photographs of the biofilm-infected wounds of the mice after different treatments (scale bar: 0.5 cm). (j) Relative wound area of biofilm-infected mice after different treatments. Reproduced with permission from ref. 95. Copyright 2024, Wiley-VCH.

physiological and pathological processes, precise regulation of ROS generation is essential for maintaining cellular homeostasis.[117,118] The structural tunability of NIR-II metal supramolecular dyes provides an ideal platform for controlled ROS release, making them promising candidates for treating ROS-related diseases. Myocardial infarction (MI)-induced ventricular arrhythmias (VAs) are the leading causes of sudden cardiac death worldwide.[119] Their occurrence is closely associated with overactivation of microglia and sympathetic neurons within the hypothalamic paraventricular nucleus (PVN), accompanied by oxidative stress, neuroinflammation, and sympathetic hyperexcitability.[120] Studies have shown that maintaining ROS levels within a sublethal range can attenuate microglial overactivation, induce protective autophagy, alleviate oxidative stress, and thereby reduce the risk of MI-related VAs.[121–123]

To address this, Sun *et al.* designed a US-activated Ru(II)-azo-BODIPY supramolecular sonosensitizer (**RuB**). This system self-assembles through coordination between an azo-BODIPY dye and half-sandwich Ru(II) acceptors to form a rectangular metallacycle (Fig. 11a).[124] Under 808 nm excitation, **RuB** exhibited strong NIR-II emission at 1110 nm, enabling deep-tissue imaging and therapy (Fig. 11b). The introduction of extended phenyl units enhanced π-conjugation, endowing **RuB** with excellent sonodynamic performance and a high $^1O_2$ quantum yield ($\Phi_\Delta = 0.88$) (Fig. 11c). Distinct from conventional SDT that relied on excessive ROS for cell ablation, **RuB** generated moderate ROS at a low concentration (5 μM) and low US power (0.5 W cm^{-2}), effectively inducing pro-survival autophagy in microglial cells. Notably, when the **RuB** concentration exceeded 5 μM or the US power surpassed 0.5 W cm^{-2}, significant apoptosis of BV2 cells occurred, indicating a well-defined ROS threshold window between autophagic activation and cell death (Fig. 11d and e). Further encapsulation of **RuB** into DSPE-PEG5000 nanoparticles (**RuB** NPs) markedly improved its biocompatibility and brain retention. *In vivo*, microinjection of **RuB** NPs into the PVN followed by localized US irradiation significantly suppressed sympathetic hyperactivity and neuroinflammation after MI, reducing the incidence of severe arrhythmias (such as SVT and VF) by approximately 60%, without detectable tissue toxicity (Fig. 11f). Mechanistically, this system modulated microglial activity *via* an ROS-triggered autophagy pathway, restoring homeostasis of the neuro–

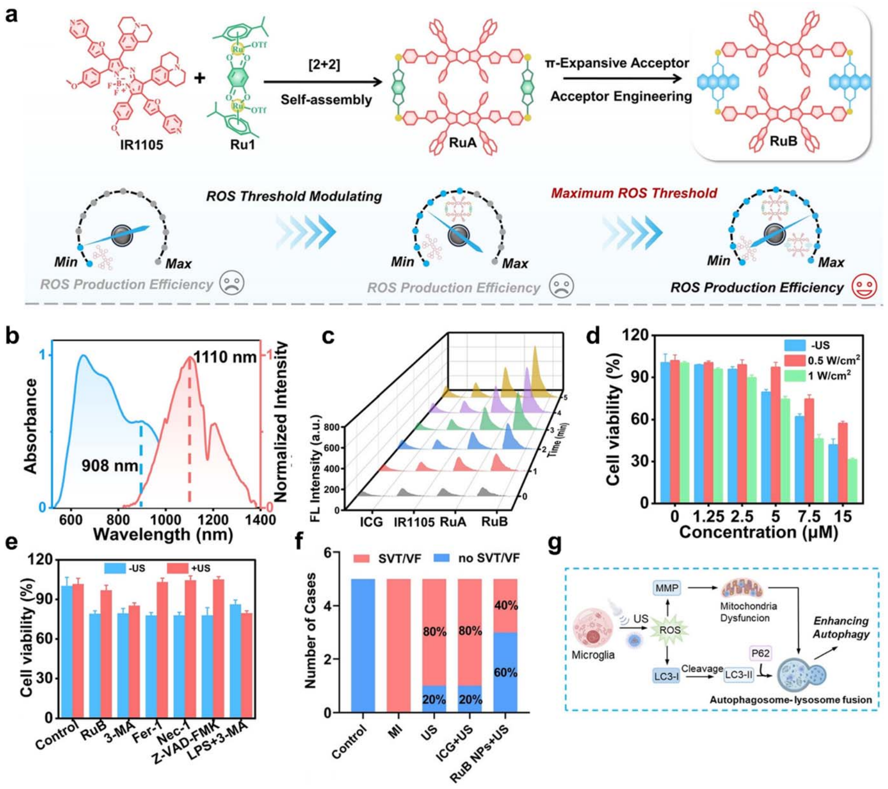

Fig. 11 (a) The design strategy of **RuB** as a sonosensitizer to regulate ROS levels and mitigate MI-induced VAs. (b) The absorption and emission spectra of **RuB**. (c) Assessment of ROS generation of various groups under US irradiation (1 W cm^{-2}) (indicator: DCFH). (d) Cell viabilities of BV2 cells incubated with **RuB** at different concentrations and different US powers (0.5 W cm^{-2} or 1 W cm^{-2}, 5 min). (e) Cell viabilities of BV2 cells co-incubated with **RuB** (5 μM) and various inhibitors under US irradiation (0.5 W cm^{-2}, 5 min). (f) Occurrence rate of SVT/VF across all experimental groups. (g) Schematic illustration of the mechanism of BV2 cell enhanced autophagy induced by RuB + US treatment. Reproduced with permission from ref. 124. Copyright 2025, Wiley-VCH.

cardiac axis and thereby reducing the risk of myocardial infarction-related mortality (Fig. 11f). This work not only broadened the scope of NIR-II metal supramolecular dyes beyond imaging and cancer therapy, but also highlights their potential for non-invasive modulation of neuro- and cardiovascular functional disorders, offering a new paradigm for adaptive ROS-guided precision medicine.

3.4 NIR-II NIR-II metal supramolecular dyes for imaging

NIR-II (1000–1700 nm) metal supramolecular dyes exhibit broad application prospects in biomedical fields due to their excellent optical properties. Compared with traditional visible light and near-infrared-I (NIR-I) fluorescence imaging, NIR-II imaging offers deeper tissue penetration, lower autofluorescence interference, and higher spatial resolution, providing unique advantages for *in vivo* vascular imaging, tumor detection, brain disease diagnosis, and surgical navigation. However, reported NIR-II luminescent supramolecular metallacages remain extremely rare, and their generally low quantum yields limit their practical application. Therefore, developing AIE-active supramolecular metallacages with efficient NIR-II luminescence for high-precision imaging at the *in vivo* level holds significant application value. Based on this, Tang developed a series of NIR-II AIE-active supramolecular metallacages, among which **MG** exhibits the most red-shifted emission at 981 nm.[102] The encapsulated nanoparticles, **MGNPs**, demonstrating high quantum yield, can still be detected with clear signals at a thickness of 6 mm (Fig. 12a). What is more, **MGNPs** highlighted the entire vascular network clearly, including fine vascular structures in the brain, hind limbs, paws, and ears. As the wavelength of the long-pass filter increased, the spatial resolution of vascular imaging was elevated with the SBR as high as 6.04 (Fig. 12b). Notably, **MGNPs** enabled clear imaging of brain vasculature by penetrating the scalp and skull, demonstrating their potential in cerebrovascular disease research (Fig. 12c).

Based on the realization of high-resolution imaging of blood vessels, the research group made further breakthroughs in subsequent studies by constructing **M-DBTP** metal cages.[101] Their outstanding imaging performance has successfully expanded the application scope of NIR-II fluorescence imaging from short-term vascular imaging to long-term analysis and even precise fluorescence-guided tumor resection. First, in terms of vascular imaging, with its NIR-II emission wavelength extending to 1006 nm, not only was higher-resolution vascular imaging achieved compared to previous work, but it also marked the first instance of metal supramolecular dyes to achieve long-term *in vivo* fluorescence tracking for up to 35 days

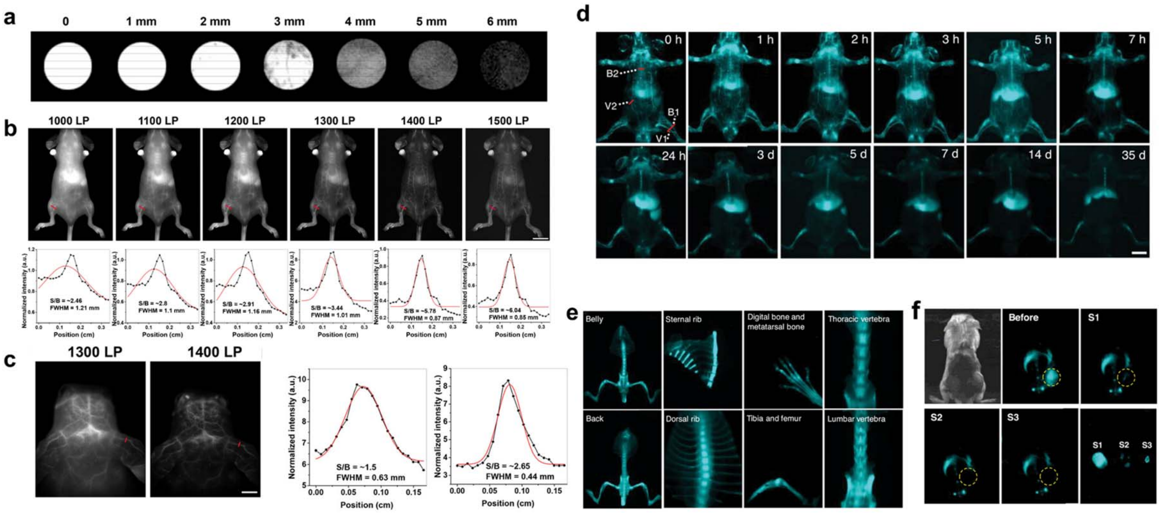

Fig. 12 (a) The fluorescence penetration depth of **MGNPs** in chicken breast. (b) NIR-II vascular fluorescence images of mice treated with **MGNPs** using different LP filters, with corresponding cross-sectional intensity profiles. The red curves represent a Gaussian fit to the dark curves. Scale bar: 1 cm. (c) NIR-II brain vascular images of mice treated with **MGNPs** using different LP filters, with corresponding cross-sectional intensity profiles of the highlighted blood vessels with red lines. The scale bar was 0.5 cm. Reproduced with permission from ref. 102. Copyright 2023, American Chemical Society. (d) The fluorescence images of the mice at different time points after **M-DBTP NPs** injection. Scale bar: 1 cm. (e) Fluorescence images of dissected bones at different sites after 3 days of **M-DBTP NPs** injection. (f) Fluorescence imaging of 4T1 tumor-bearing mice before and after three surgeries, with corresponding dissected tumor images. Reproduced with permission from ref. 101. Copyright 2025, Wiley-VCH.

(Fig. 12d). For the first time, NIR-II fluorescence imaging technology visually revealed the unique metabolic pathway of supramolecular metallacage nanoparticles, which are rapidly cleared from the bloodstream and then specifically accumulate and persistently reside in the bone marrow region (Fig. 12e). These findings were highly consistent with the Pt distribution detected by ICP-OES. Finally, leveraging the enhanced permeability and retention (EPR) effect of **M-DBTP** NPs in 4T1 tumor-bearing mice, NIR-II fluorescence imaging-guided tumor surgery was successfully achieved (Fig. 12f). By monitoring residual fluorescence signals during surgery, precise and complete resection of tumor tissue was accomplished, demonstrating its significant potential in cancer precision therapy.

4 Conclusions and perspective

Developing molecular tools for early diagnosis and intervention is pivotal to precision medicine.[125–127] Metal supramolecular dyes feature tunable photophysical properties, enhanced photosensitization, improved cellular internalization, and strong resistance to ACQ. Notably, metal supramolecular dyes can often be constructed in a modular and operationally simple manner, avoiding laborious multistep synthesis and purification. These advantages have already driven substantial progress in biomedicine, positioning metal supramolecular dyes as compelling alternatives to conventional small-molecule fluorophores.

To date, however, most metal supramolecular dyes operate in the visible region, which restricts their use in deep-tissue applications. Against this backdrop, our group has focused on developing NIR-II metal supramolecular dyes and achieved notable advances in bioimaging and disease therapy. Early efforts relied on amphiphilic encapsulation to co-load NIR-II fluorophores with visible-light metal supramolecular dyes into nanoparticles. This strategy suffered from payload leakage, leading to a lack of synchrony between fluorescence reporting and therapeutic action. These limitations motivated the development of NIR-II metal supramolecular dyes that are constructed directly through coordination-driven self-assembly between NIR-II ligands and metal acceptors. Most NIR-II ligands used to date are based on aza-BODIPY, D–A–D, or AIE scaffolds, which typically exhibit NIR-II fluorescence accompanied by photosensitizing and photothermal capabilities, which can be further amplified upon self-assembly forming metal supramolecular dyes. Over the past five years, NIR-II metal supramolecular dyes have expanded rapidly, yet several bottlenecks still remain, restricting their further development.

The number of reported NIR-II metal supramolecular dyes is still limited: ligands are dominated by D–A–D and BODIPY frameworks, while acceptors largely rely on Ru(II) and Pt(II) centers. This limited chemical option stems partly from the scarcity of NIR-II fluorophore motifs and partly from reduced assembly efficiency associated with enlarged π-conjugated surfaces. There is therefore a pressing need for general design principles that maintain reliable self-assembly while enabling the co-optimization of NIR-II emission with therapy-relevant functions, thereby broadening the molecular library of NIR-II metal supramolecular dyes. In this context, AI- and data-driven screening could help prioritize promising structures and assembly conditions, reducing empirical trial-and-error and accelerating development of NIR-II metal supramolecular dyes. Sustained efforts should be devoted to AI-enabled rational design of NIR-II metal supramolecular dyes, aiming to build more diverse molecular libraries for exploring structure-activity relationships and potential biomedical applications.

Biosensing refers to molecular probes that alter their optical outputs in response to specific stimuli (*e.g.*, light, acoustic fields, small molecules, or biomacromolecules), thereby reporting analyte changes at the molecular level and enabling semi-quantitative analysis. Current NIR-II metal supramolecular dyes are predominantly "always-on" emitters and are thus poorly suited to tracking dynamic pathological microenvironment changes. Leveraging the anti-quenching advantage of macrocyclic architectures, activatable NIR-II metal supramolecular dyes could be engineered to provide more accurate diagnosis and therapy, which directly support the goals of precision medicine.

The key advantage of NIR-II metal supramolecular dyes lies in biomedicine, where stability under physiological conditions is essential for retaining bioactivity. NIR-II metal supramolecular dyes are assembled through noncovalent interactions and many incorporate large, hydrophobic π-conjugated frameworks, resulting in poor stability in biological media. Although coating MIR-II metal supramolecular dyes with amphiphilic materials can improve *in vivo* stability and biocompatibility, the cellular uptake, biodistribution, and metabolic clearance of encapsulated metal supramolecular dyes differ substantially from those of the original supramolecular species. This discrepancy complicates mechanistic studies of how metal supramolecular dyes function *in vivo*. Therefore, developing intrinsically stable NIR-II metal supramolecular dyes remains a pressing need. Introducing multivalent assembly motifs by incorporating additional noncovalent interactions beyond coordination holds significant potential to enhance supramolecular robustness. Moreover, metal acceptors used in current NIR-II metal supramolecular dyes have largely been limited to Pt and Ru. Expanding to other metal platforms may provide new stabilization motifs and further improve supramolecular robustness.

The intrinsic metal-associated biotoxicity of metal supramolecular dyes severely limits their biomedical translation. This issue may be mitigated by modifying donors and acceptors to introduce shielding elements that reduce undesirable interactions between the metal center and biomolecules. Alternatively, replacing heavy-metal centers with lighter metals can circumvent heavy-metal toxicity and depress ISC, which can enhance fluorescence quantum yields, benefiting high-resolution deep-tissue imaging.

In the future, NIR-II metal supramolecular dyes could be employed in expanded biomedical applications, including NIR-II imaging-guided radiosensitization therapy and *in situ* self-assembly *in vivo*. (1) Radiosensitization aims to enhance radiotherapy efficacy by amplifying radiation-induced DNA damage in tumor tissues.[128] Metal supramolecular dyes represent ideal radiosensitizing platforms. The high-Z metal centers (*e.g.*, Pt and Ru) of metal supramolecular dyes allow effective absorption of X-rays for further radiosensitization and depositing radiation energy into tumors.[129,130] The integration of radio-therapy into NIR-II metal supramolecular dyes enables precise tracking using NIR-II emitters, facilitating guided treatment. (2) *In situ* self-assembly, which builds complexes directly at the target site *via* monomer biochemical reactions, significantly improved the performance of drug delivery systems for disease therapy and imaging.[131,132] The nature of metal supramolecular dyes, formed through dynamic self-assembly, makes them potential candidates for realizing *in situ* assembly. It can effectively avoid the systemic toxicity arising from heavy atoms and stimuli of ROS-mediated dynamic therapies for normal tissues and maximize the NIR-II imaging efficacy. Thus, designing *in situ* assembled metal supramolecular dyes is meaningful.

Author contributions

Y. Sun, Y. Tang, and X. Xiong supervised this work. F. Zhao, Q. Song, and P. Qiu conceived the idea and wrote the manuscript. F. Zhao participated in the literature survey. F. Zhao commented on the manuscript.

Conflicts of interest

There are no conflicts to declare.

Data availability

No primary research results, software or code have been included and no new data were generated or analysed as part of this review.

Acknowledgements

We thank the National Natural Science Foundation of China (22374055, 22022404 and 22204055), the National Natural Science Foundation of Hubei Province (2022CFA033), the Fundamental Research Funds for the Central Universities (CCNU24CG013, CCNU24JCPT001, CCNU24JCPT020, and CCNU30106240021), and the National Natural Science Foundation of China (No. 21806048).

Notes and references

1 C. Lin, M. Lo, R. Moody, H. Jiang, R. Harouaka, N. Stevers, S. Tinsley, M. Gasparyan, M. Wicha and D. Sun, *Cancer Lett.*, 2018, **438**, 165–173.
2 S. L. Bacon, Stress, psychiatric. disorders, and cardiovascular disease, *BMJ*, 2019, **365**, l1577.
3 N. Conrad, G. Verbeke, G. Molenberghs, L. Goetschalckx, T. Callender, K. Rahimi, J. Mason, J. V. McMurray and J. Verbakel, *Eur. Heart J.*, 2022, **43**, ehac544.2862.
4 J. Chen, N. Dadheech and E. H. P. Tan, *Nat. Med.*, 2025, **31**, 2147–2160.
5 T. Tsujimoto, T. Sugiyama, M. Noda and H. Kajio, *Diabetes Care*, 2016, **39**, 1818–1826.
6 K. F. Budden, S. D. Shukla, S. F. Rehman, K. L. Bowerman, S. Keely, P. Hugenholtz, D. P. H. Armstrong-James,

I. M. Adcock, S. H. Chotirmall, K. Chung and P. M. Hansbro, *Lancet Respir. Med.*, 2019, **7**, 907–920.

7 B. A. Aguado, J. C. Grim, A. M. Rosales, J. J. Watson-Capps and K. S. Anseth, *Sci. Transl. Med.*, 2018, **10**, eaam8645.

8 H. Li and R. Zhan, *Front. Public Health*, 2024, **12**, 1425716.

9 S. K. Shukla, N. S. Murali and M. H. Brilliant, *Trends Mol. Med.*, 2015, **21**, 461–462.

10 W. Fu, S. Zhao, Y. Zhang, P. Chai and J. Goss, *Br. Med. J.*, 2018, **360**, k234.

11 X. Wang, Y. Qi and Z. Hu, *Adv. Compos. Hybrid Mater.*, 2022, **5**, 1786–1798.

12 X. Wang, S. Liew, J. Huang, Y. Hu, X. Wei and K. Pu, *J. Am. Chem. Soc.*, 2024, **146**, 22689–22698.

13 Y. Lin, J. Huang, J. Liu, M. Xu, C. Xu and K. Pu, *J. Am. Chem. Soc.*, 2025, **147**, 2597–2606.

14 H. Yang, Z. Yan and X. Liu, *Nat. Protoc.*, 2025, **19**, 1336–134.

15 S. Zuo, H. Liu, G. Jiang, Y. Chen, T. Ren, Z. Zhou, X. Zhang and L. Yuan, *J. Am. Chem. Soc.*, 2025, **147**, 42825–42838.

16 J. Han, M. Yang, C. Lv, K. Li, J. Fan and X. Peng, *Chem. Sci.*, 2026, **17**, 2791–2801.

17 Y. Kuriki, T. Yoshioka, M. Kamiya, T. Komatsu, H. Takamaru, K. Fujita, H. Iwaki, A. Nanjo, Y. Akagi, K. Takeshita, H. Hino, R. Hino, R. Kojima, T. Ueno, K. Hanaoka, S. Abe, Y. Saito, J. Nakajima and Y. Urano, *Chem. Sci.*, 2022, **13**, 4474–4481.

18 Y. Ye, J. Pan, H. Wang, X. Zhang, H. Zhu and X. Liu, *Chem. Soc. Rev.*, 2024, **53**, 9133–9189.

19 H. Zheng, X. Zhan, Q. Bian and X. Zhang, *Chem. Commun.*, 2013, **49**, 429–447.

20 E. Noelting and K. Dziewonsky, *Ber. Dtsch. Chem. Ges.*, 1905, **38**, 3516.

21 K. Yan, Z. Hu, P. Yu, Z. He, Y. Chen, J. Chen, H. Sun, S. Wang and F. Zhang, *Nat. Commun.*, 2024, **15**, 2593.

22 A. L. Antaris, H. Chen, K. Cheng, Y. Sun, G. Hong, C. Qu, S. Diao, Z. Deng, X. Hu, B. Zhang, X. Zhang, O. Yaghi, Z. R. Alamparambil, X. Hong, Z. Cheng and H. Dai, *Nat. Mater.*, 2016, **15**, 235–242.

23 L. Manen, H. J. M. Handgraaf, M. Diana, J. Dijkstra, T. Ishizawa, A. L. Vahrmeijer and J. S. D. Mieog, *J. Surg. Oncol.*, 2018, **118**, 283–300.

24 K. Jiang, B. Luo, Z. Hou, C. Li, H. Cai, J. Tang and G. Yao, *Ann. Transl. Med.*, 2021, **9**, 1456.

25 Q. Yang and X. Zhang, *BMC Surg.*, 2023, **23**, 133.

26 C. J. Pedersen, *J. Am. Chem. Soc.*, 1967, **89**, 7017–7036.

27 D. J. Cram, *Angew. Chem., Int. Ed.*, 1988, **27**, 1009–1020.

28 J. M. Lehn, *Angew. Chem., Int. Ed.*, 1988, **27**, 89–112.

29 C. O. Dietrich-Buchecker, J. P. Sauvage and J. M. Kern, *J. Am. Chem. Soc.*, 1984, **106**, 3043–3045.

30 H. Li, M. Eddaoudi and M. O'Keeffe, *Nature*, 1999, **402**, 276–27.

31 K. Iizuka, H. Takezawa and M. Fujita, *J. Am. Chem. Soc.*, 2024, **146**, 32311–32316.

32 S. Liu, N. Kishida, J. Kim, N. Fukui, R. Haruki, Y. Niwa, R. Kumai, D. Kim, M. Yoshizawa and H. Shinokubo, *J. Am. Chem. Soc.*, 2023, **145**, 2135–2141.

33 A. Mukherjee, S. Barman, A. Ghosh, S. Chakraborty, A. Datta, A. Datta and S. Ghosh, *Chem. Sci.*, 2022, **13**, 781–788.

34 I. Insua, A. Cardellini, S. Díaz, J. Bergueiro, R. Capelli, G. M. Pavan and J. Montenegro, *Chem. Sci.*, 2023, **14**, 14074–14081.

35 Q. Wu, Z. Zhou, L. Xu, H. Zhong, B. Xiong, T. Ren, Z. Li, L. Yuan and X. Zhang, *Sci. Adv.*, 2024, **10**, eadp8719.

36 J. Zhang, Y. Hu, X. Wen, Z. Yang, Z. Wang, Z. Feng, H. Bai, Q. Xue, Y. Miao, T. Tian, P. Zheng, J. Zhang, J. Li, L. Qiu, J. Xu and D. Ye, *Nat. Nanotechnol.*, 2025, **20**, 563–574.

37 P. J. Stang and D. Cao, *J. Am. Chem. Soc.*, 1994, **116**, 4981–4982.

38 Y. Sun, C. Chen, J. Liu and P. J. Stang, *Chem. Soc. Rev.*, 2020, **49**, 3889–3919.

39 G. Yu, S. Yu, M. L. Saha, J. Zhou, T. R. Cook, B. C. Yung, J. Chen, Z. Mao, F. Zhang, Z. Zhou, Y. Liu, L. Shao, S. Wang, C. Gao, F. Huang, P. J. Stang and X. Chen, *Nat. Commun.*, 2018, **9**, 4335.

40 Z. Li, X. Yan, F. Huang, H. Sepehrpour and P. J. Stang, *Org. Lett.*, 2017, **19**, 5728–5731.

41 Z. Zhou, J. Liu, J. Huang, T. W. Rees, Y. Wang, H. Wang, X. Li, H. Chao and P. J. Stang, *Proc. Natl. Acad. Sci. U. S. A.*, 2019, **116**, 20296–20302.

42 J. Zhou, Y. Zhang, G. Yu, M. R. Crawley, C. R. P. Fulong, A. E. Friedman, S. Sengupta, J. Sun, Q. Li, F. Huang and T. R. Cook, *J. Am. Chem. Soc.*, 2018, **140**, 7730–7736.

43 R. Chakrabarty, P. S. Mukherjee and P. J. Stang, *Chem. Rev.*, 2011, **111**, 6810–6918.

44 Y. Ding, Z. Tong, L. Jin, B. Ye, J. Zhou, Z. Sun, H. Yang, L. Hong, F. Huang and W. Wang, *Adv. Mater.*, 2022, **34**, 2106388.

45 Y. Yuan, S. Diao, X. Ni, D. Zhang, W. Yi, C. Jian, X. Hu, D. Li, A. Yu and W. Zhou, *J. Nanobiotechnol.*, 2022, **20**, 44.

46 Y. Sun, F. Ding, Z. Chen, R. Zhang, C. Li, Y. Xu, Y. Zhang, R. Ni, X. Li, G. Yang, Y. Sun and P. J. Stang, *Proc. Natl. Acad. Sci. U. S. A.*, 2019, **116**, 16729–16735.

47 S. Fang, M. Wang, C. Tang, G. Wu, E. Liu, H. Han, B. Zhao, S. Li, M. Xiao and M. Li, *CCS Chem.*, 2025, **7**, 3015–3024.

48 Y. Qin, Q. Ling, Y. Wang, Y. Hu, L. Hu, X. Zhao, D. Wang, H. Yang, L. Xu and B. Tang, *Angew. Chem., Int. Ed.*, 2023, **62**, e202308210.

49 X. Li, J. F. Lovell, J. Yoon and X. Chen, *Nat. Rev. Clin. Oncol.*, 2020, **17**, 657.

50 H. Sepehrpour, W. Fu, Y. Sun and P. J. Stang, *J. Am. Chem. Soc.*, 2019, **141**, 14005–14020.

51 I. V. Grishagin, J. B. Pollock, S. Kushal, T. R. Cook, P. J. Stang and B. Z. Olenyuk, *Proc. Natl. Acad. Sci. U. S. A*, 2014, **111**, 18448–18453.

52 L. Tu, C. Li, C. Liu, S. Bai, J. Yang, X. Zhang, L. Xu, X. Xiong and Y. Sun, *Chem. Commun.*, 2022, **58**, 9068–9071.

53 Z. Zhou, J. Liu, J. Huang, T. W. Rees, Y. Wang, H. Wang, X. Li, H. Chao and P. J. Stang, *Proc. Natl. Acad. Sci. U. S. A*, 2019, **116**, 20296–20302.

54 L. He, L. Cai, M. Li, G. Zhang, L. Zhou, T. Chen, M. Lin and Q. Sun, *Chem. Sci.*, 2020, **11**, 940–7949.

55 G. Li, X. Zhang, W. Zhao, W. Zhao, F. Li, K. Xiao, Q. Yu, S. Liu and Q. Zhao, *ACS Appl. Mater. Interfaces*, 2020, **12**, 20180–20190.

56 B. Huang, X. Liu, G. Yang, J. Tian, Z. Liu, Y. Zhu, X. Li, G. Yin, W. Zheng, L. Xu and W. Zhang, *CCS Chem.*, 2022, **4**, 2090–2101.

57 X. Lin, F. Chen, X. Yu, H. Wang, H. Qiu, Y. Li, S. Yin and P. J. Stang, *Proc. Natl. Acad. Sci. U. S. A.*, 2022, **119**, e2203994119.

58 G. Hong, A. L. Antaris and H. Dai, *Nat. Biomed. Eng.*, 2017, **1**, 0010.

59 A. L. Antaris, H. Chen, S. Diao, Z. Ma, Z. Zhang, S. Zhu, J. Wang, A. X. Lozano, Q. Fan, L. Chew, M. Zhu, K. Cheng, X. Hong, H. Dai and Z. Cheng, *Nat. Commun.*, 2017, **8**, 15269.

60 Z. Guo, S. Park, J. Yoon and I. Shin, *Chem. Soc. Rev.*, 2014, **43**, 16–29.

61 T. Ren, Z. Wang, Z. Xiang, P. Lu, H. Lai, L. Yuan, X. Zhang and W. Tan, *Angew. Chem., Int. Ed.*, 2021, **60**, 800.

62 W. Huang, H. Yang, Z. Hu, Y. Fan, X. Guan, W. Feng, Z. Liu and Y. Sun, *Adv. Healthcare Mater.*, 2021, **10**, 2101003.

63 F. Heinemann, J. Karges and G. Gasser, *Acc. Chem. Res.*, 2017, **50**, 2727.

64 Y. Yang, Y. Liu, J. Weng, X. Wen, Y. Liu and D. Ye, *Biomaterials*, 2024, **305**, 122454.

65 Q. Ding, X. Hong, Z. Cheng and J. S. Kim, *CCS Chem.*, 2025, **7**, 2899–2911.

66 Y. Ding, Z. Tong, L. Jin, B. Ye, J. Zhou, Z. Sun, H. Yang, L. Hong, F. Huang, W. Wang and Z. Mao, *Adv. Mater.*, 2022, **34**, 2106388.

67 Y. Sun, F. Ding, Z. Zhou, C. Li, M. Pu, Y. Xu, Y. Zhan, X. Lu, H. Li, G. Yang, Y. Sun and P. J. Stang, *Proc. Natl. Acad. Sci. U. S. A.*, 2019, **116**, 1968.

68 F. Ding, Z. Chen, W. Y. Kim, A. Sharma, C. Li, Q. Ouyang, H. Zhu, G. Yang, Y. Sun and J. S. Kim, *Chem. Sci.*, 2019, **10**, 7023–7028.

69 A. Loudet and k. Burgess, *Chem. Rev.*, 2007, **107**, 4891–4932.

70 G. Ulrich, R. Ziessel and A. Harriman, *Angew. Chem., Int. Ed.*, 2008, **47**, 1184–1201.

71 J. M. Franke, B. K. Raliski, S. C. Boggess, D. V. Natesan, E. T. Koretsky, P. Zhang, R. U. Kulkarni, P. E. Deal and E. W. Miller, *J. Am. Chem. Soc.*, 2019, **141**, 12824–12831.

72 S. Wijesooriya, J. A. Peterson, P. Shrestha, E. J. Gehrmann, A. H. Winter and E. A. Smith, *Angew. Chem., Int. Ed.*, 2018, **57**, 12685.

73 J. Shao, H. Sun, H. Guo, S. Ji, J. Zhao, W. Wu, X. Yuan, C. Zhang and T. D. James, *Chem. Sci.*, 2012, **3**, 1049–1061.

74 Y. Chen, J. Zhao, H. Guo and L. Xie, *Org. Chem.*, 2012, **77**, 2192–2206.

75 Y. Liu and G. Liu, *Angew. Chem., Int. Ed.*, 2023, **62**, e202309786.

76 S. Wu and W. Zhang, *Chem. Sci.*, 2024, **15**, 5973–5979.

77 S. Hu, W. Zhang, Z. Ni, L. Tian, J. Tian, H. Lu and L. Gai, *Chin. Chem. Lett.*, 2025, 111523.

78 J. Lin, X. Zeng and Y. Xiao, *Chem. Sci.*, 2019, **10**, 1219–1226.

79 Y. Xu, C. Li, S. Lu, Z. Wang, S. Liu, X. Yu, X. Li and Y. Sun, *Nat. Commun.*, 2022, **13**, 2009.

80 C. Li, Y. Xu, L. Tu, M. Choi, Y. Fan, X. Chen, J. L. Sessler, J. S. Kim and Y. Sun, *Chem. Sci.*, 2022, **13**, 6541–6549.

81 L. Tu, C. Li, X. Xiong, J. H. Kim, Q. Li, L. Mei, J. Li, S. Liu, J. S. Kim and Y. Sun, *Angew. Chem., Int. Ed.*, 2023, **135**, e202301560.

82 C. Li, L. Tu, J. Yang, C. Liu, Y. Xu, J. Li, W. Tuo, B. Olenyuk, Y. Sun, P. J. Stang and Y. Sun, *Chem. Sci.*, 2023, **14**, 2901–2909.

83 Y. Xu, C. Li, J. An, X. Ma, J. Yang, L. Luo, Y. Deng, J. S. Kim and Y. Sun, *Sci. China:Chem.*, 2023, **66**, 155–163.

84 C. Li, L. Tu, Y. Xu, M. Li, J. Du, P. J. Stang, Y. Sun and Y. Sun, *Angew. Chem., Int. Ed.*, 2024, **136**, e202406392.

85 X. Li, Y. Yang, R. Zhang and W. Huang, *Chem. Soc. Rev.*, 2025, **54**, 11184–11225.

86 Y. Chen, L. Xue, Q. Zhu, Y. Feng and M. Wu, *Front. Chem.*, 2021, **9**, 750404.

87 A. Ji, H. Lou and C. Qu, *Nat. Commun.*, 2022, **13**, 3815.

88 Q. Qiu, T. Chang and Y. Wu, *Biosens. Bioelectron.*, 2022, **212**, 114371.

89 Y. Sun, F. Ding, Z. Zhou, C. Li, M. Pu, Y. Xu, Y. Zhan, X. Lu, H. Li and G. Yang, *Proc. Natl. Acad. Sci. U. S. A.*, 2019, **116**, 1968–1973.

90 Y. Sun, M. Ding, X. Zeng, Y. Xiao, H. Wu and H. Zhou, *Chem. Sci.*, 2017, **8**, 3489–3493.

91 Q. Yang, Z. Hu and S. Zhu, *J. Am. Chem. Soc.*, 2018, **140**, 1715–1724.

92 C. Liu, M. Li, H. Ma, Z. Hu, X. Wang, R. Ma, Y. Jiang, H. Sun, S. Zhu and Y. Liang, *Research*, 2023, **6**, 0039.

93 Y. Xu, C. Li, X. Ma, W. Tuo, L. Tu, X. Li, Y. Sun, P. J. Stang and Y. Sun, *Proc. Natl. Acad. Sci. U. S. A.*, 2022, **119**, e2209904119.

94 Y. Fan, C. Li, S. Bai, X. Ma, J. Yang, X. Guan and Y. Sun, *Small*, 2022, **18**, 2201625.

95 Y. Xu, Y. Pang, L. Luo, A. Sharma, J. Yang, C. Li, S. Liu, J. Zhan and Y. Sun, *Angew. Chem., Int. Ed.*, 2024, **63**, e202319966.

96 Y. Pang, Y. Luo, T. Liu, Q. Li, L. Mei, J. Zhang, C. Li, J. Li and Y. Sun, *Chem. Sci.*, 2025, **16**, 19632–19643.

97 J. Luo, Z. Xie, J. Lam, L. Cheng, H. Chen, C. Qiu, H. S. Kwok, X. Zhan, Y. Liu and D. Zhu, *Chem. Commun.*, 2001, **18**, 1740–1741.

98 P. Das, A. Kumar, A. Chowdhury and P. S. Mukherjee, *ACS Omega*, 2018, **3**, 13757–13771.

99 Z. Wang, J. Nie, W. Qin, Q. Hu and B. Tang, *Nat. Commun.*, 2016, **7**, 12033.

100 Y. Qin, X. Chen, Y. Gui, H. Wang, B. Tang and D. Wang, *J. Am. Chem. Soc.*, 2022, **144**, 12825–12833.

101 Y. Qin, N. Niu, X. Li, X. Yan, S. Lu, Z. Li, Y. Gui, J. Zhu, L. Xu, X. Li, D. Wang and B. Tang, *Aggregate*, 2025, **6**, e708.

102 Y. Qin, X. Li, S. Lu, M. Kang, Z. Zhang, Y. Gui, X. Li, D. Wang and B. Tang, Acs, *Mater. Lett.*, 2023, **5**, 1982–1991.

103 P. Liang, L. Ren, Y. Yan, Z. Li, F. Yang, T. Ren, L. Yuan and X. Zhang, *Angew. Chem., Int. Ed.*, 2025, **64**, e202419376.

104 Y. Cai, T. Chai, W. Nguyen, J. Liu, E. Xiao, X. Ran, Y. Ran, D. Du, W. Chen and X. Chen, *Signal Transduction Targeted Ther.*, 2025, **10**, 115.

105 D. Xi, M. Xiao, J. Cao, L. Zhao, N. Xu, S. Long, J. Fan, K. Shao, W. Sun, X. Yan and X. Peng, *Adv. Mater.*, 2020, **32**, 1907855.

106 Q. Ding, L. Zhou, T. Xiong, J. Liu, L. Chen, J. Yoo, X. Xu, X. Jia, S. Chen and S. Chen, *Natl. Sci. Rev.*, 2025, nwaf554.

107 L. Liu, J. Zhang, R. An, Q. Xue, X. Cheng, Y. Hu, Z. Huang, L. Wu, W. Zeng, Y. Miao, J. Li, Y. Zhou, H. Chen, H. Liu and D. Ye, *Angew. Chem., Int. Ed.*, 2023, **62**, e20221705.

108 L. Wu, Y. Liu, W. Zeng, Y. Ishigaki, S. Zhou, X. Wang, Y. Sun, Y. Zhang, X. Jiang, T. Suzuki and D. Ye, *J. Am. Chem. Soc.*, 2023, **145**, 27838–27849.

109 L. Tu, C. Li, Q. Ding, A. Sharma, M. Li, J. Li, J. S. Kim and Y. Sun, *J. Am. Chem. Soc.*, 2024, **146**, 8991–9003.

110 Y. Xu, Y. Zhang, J. Li, J. An, C. Li, S. Bai, A. Sharma, G. Deng, J. S. Kim and Y. Sun, *Biomaterials*, 2020, **259**, 120315.

111 S. Gao, X. Yan, G. Xie, M. Zhu, X. Ju, P. J. Stang, Y. Tian and Z. Niu, *Proc. Natl. Acad. Sci. U. S. A.*, 2019, **116**, 23437–23443.

112 K. C. King, R. B. Stelkens, J. P. Webster, D. F. Smith and M. A. Brockhurst, *PLoS Pathog.*, 2015, **11**, e1005098.

113 Y. Huang, W. Chen, J. Chung, J. Yin and J. Yoon, *Chem. Soc. Rev.*, 2021, **50**, 7725–7744.

114 M. Kang, C. Zhou, S. Wu, B. Yu, Z. Zhang, N. Song, M. M. S. Lee, W. Xu, F.-J. Xu and D. Wang, *J. Am. Chem. Soc.*, 2019, **141**, 16781–16789.

115 Y. Zhang, Q. Wang, Z. Zhu, W. Zhao, C. Yan, Z. Liu, M. Liu, X. Zhao, H. Tian and W. Zhu, *CCS Chem.*, 2022, **4**, 1619–1632.

116 Y. Yang, X. Fan, L. Li, Y. Yang, A. Nuernisha, D. Xue, C. He, J. Qian, Q. Hu, H. Chen, J. Liu and W. Huang, *ACS Nano*, 2020, **14**, 2509–2521.

117 C. Lennicke and H. M. Cochemé, *Mol. Cell*, 2021, **81**, 3691–3707.

118 L. A. Sena, S. Li, A. Jairaman, M. Prakriya, T. Ezponda, D. A. Hildeman, C. Wang, P. T. Schumacker, J. D. Licht and H. Perlman, *Immunity*, 2013, **38**, 225–236.

119 R. M. John, U. B. Tedrow, B. A. Koplan, C. M. Albert, L. M. Epstein, M. O. Sweeney, A. L. Miller, G. F. Michaud and W. G. Stevenson, *Lancet*, 2012, **380**, 1520–1529.

120 Y. Wang, H. Hu, J. Yin, Y. Shi, J. Tan, L. Zheng, C. Wang, X. Li, M. Xue and J. Liu, *Redox Biol.*, 2019, **24**, 101186.

121 C. Wang, W. Du, C. Wu, S. Dan, M. Sun, T. Zhang, B. Wang, Y. Yuan and G. Liang, *Angew. Chem., Int. Ed.*, 2022, **61**, e202114766.

122 B. Van den Broek, I. Pintelon, I. Hamad, S. Kessels, M. Haidar, N. Hellings, J. J. Hendriks, M. Kleinewietfeld, B. Brône and V. Timmerman, *J. Extracell. Vesicles*, 2020, **10**, e12022.

123 J. Huang, J. Sun, Y. Wu and C. Turro, *J. Am. Chem. Soc.*, 2021, **143**, 1610–1617.

124 Y. Pang, Q. Li, J. Wang, S. Wang, A. Sharma, Y. Xu, H. Hu, J. Li, S. Liu and Y. Sun, *Angew. Chem., Int. Ed.*, 2025, **64**, e202415802.

125 D. Sar, F. Ostadhossein, P. Moitra, M. Alafeef and D. Pan, *Adv. Sci.*, 2022, **9**, 2202414.

126 H. Wang, H. Liu, W. Li, S. Li, J. Zhang, J. Zang, L. Liu and P. Wang, *Chem. Sci.*, 2024, **15**, 11347–11357.

127 Z. Li, P. Liang, L. Xu, X. Zhang, K. Li, Q. Wu, X. Lou, T. Ren, L. Yuan and X. Zhang, *Nat. Commun.*, 2023, **14**, 1843.

128 Y. Tian, L. Wang, R. Chen, Y. Miao, Y. Liu, W. Huang, L. Fang, S. Liu, J. Luo, X. Sun, Y. Zhang and D. Ye, *Angew. Chem., Int. Ed.*, 2025, **64**, e202500645.

129 Y. Wang, X. Duan, Y. Huang, Y. Hou, K. Wu, F. Zhang, M. Pan, J. Shen and C. Su, *ACS Appl. Mater. Interfaces*, 2023, **15**, 43479–43491.

130 B. Lv, H. Zhang, X. Zheng, H. Wang, W. Ge, Y. Ren, Z. Tan, M. Zhang, Z. Tang, Y. Liu, L. Zhang, Y. Wu, X. Jiang and W. Bu, *Nano Today*, 2020, **35**, 100988.

131 J. Kim, S. Lee, Y. Kim, M. Choi, I. Lee, E. Kim, C. G. Yoon, K. Pu, H. Kang and J. S. Kim, *Nat. Rev. Mater.*, 2023, **8**, 710–725.

132 Z. Cao, D. Li, L. Zhao, M. Liu, P. Ma, Y. Luo and X. Yang, *Nat. Commun.*, 2022, **13**, 2038.